

# Numerical Methods for Solving Nonlinearly Coupled Poisson Equations in Dual-Continuum Modeled Porous Electrodes

Yuhe Wang\*

Min Wang<sup>†‡</sup>

Zhihang Xu<sup>§</sup>

July 31, 2025

## Abstract

Porous electrodes are widely used in electrochemical systems, where accurately determining electric potentials, particularly overpotentials, is essential for understanding electrode behavior. At the macroscopic scale, porous electrodes are typically modeled using a dual-continuum approach, treating the porous solid phase and the liquid electrolyte as spatially superimposed domains. Determining potential distributions requires solving two Poisson equations that are nonlinearly coupled through Butler-Volmer kinetics under galvanostatic and potentiostatic operating modes. Under galvanostatic operation, these equations form an underconstrained singular system due to all-Neumann boundary conditions, posing numerical challenges. This paper systematically presents numerical methods for solving nonlinearly coupled Poisson equations in dual-continuum porous electrodes, with a particular focus on galvanostatic solutions. We mathematically establish solution uniqueness in terms of the potential difference between the electrode and electrolyte (or overpotential), as well as the individual potentials up to a shared constant shift. To resolve the nonuniqueness of the solution, we introduce three numerical approaches: (1) Lagrange Constrained Method (LCM), (2) Dirichlet Substitution Method (DSM), and (3) Global Constraining Method (GCM), where GCM enables solving the overpotential without imposing an explicit system reference potential. Additionally, we develop both decoupled and fully coupled nonlinear solution strategies and evaluate their computational performance in both homogeneous and heterogeneous conductivity cases. The presented numerical methods are general for addressing similar underconstrained nonlinear systems. A Python implementation is provided at [https://github.com/harrywang1129/porous\\_electrode\\_solver](https://github.com/harrywang1129/porous_electrode_solver).

**Keywords:** Porous Media, Poisson Equations, Nonlinear Coupling, Underconstrained PDE, Numerical Methods, Electric Potential Fields

## 1 Introduction

Porous electrodes play a crucial role in many electrochemical energy storage devices [1, 2]. Their large surface area and interconnected pore structures facilitate efficient electrochemical reactions and mass

\*Institute for Scientific Computation, Texas A&M University, College Station, TX 77843, USA. [yuhe.wang@tamu.edu](mailto:yuhe.wang@tamu.edu)

<sup>†</sup>Department of Mathematics, University of Houston, Houston, TX 77204, USA. [mwang55@central.uh.edu](mailto:mwang55@central.uh.edu)

<sup>‡</sup>Corresponding author

<sup>§</sup>Department of Mathematics, University of Houston, Houston, TX 77204, USA. [zxu29@central.uh.edu](mailto:zxu29@central.uh.edu)

transport, both of which are critical to device performance. The efficiency of porous electrodes arises from the intricate interplay among ionic transport in the electrolyte, electronic conduction in the solid electrode phase, and electrochemical reactions occurring at the electrode-electrolyte interfaces within the porous structure [3, 4, 5, 6]. Understanding and optimizing these coupled processes are essential for advancing the design and performance of electrochemical energy storage devices, including batteries, flow cells, and supercapacitors [7, 8]. A key aspect of this is accurately modeling the electric potential fields in both the solid electrode and liquid electrolyte phases, as these fields dictate the localized distribution of electrochemical reaction rates and ultimately influence overall device efficiency [9, 10].

The continuum approach is commonly used for porous electrode modeling at the macroscopic level [11, 12, 13], where spatiotemporal variables are represented using “mean-field” approximations. In this framework, the electrode and electrolyte potential domains are superimposed, resulting in a system of coupled Poisson equations governed by charge conservation and electrochemical kinetics. The corresponding coupled potential field model for the porous electrode system is typically written in the following closure form [14, 15, 16]:

$$\nabla \cdot (-\sigma \nabla \phi_e) = \nabla \cdot \vec{j}_e \quad \text{in } \Omega_e, \quad (1a)$$

$$\nabla \cdot (-\kappa \nabla \phi_l) = \nabla \cdot \vec{j}_l \quad \text{in } \Omega_l, \quad (1b)$$

where the two Poisson equations (**Eqs. (1a) and (1b)**) are nonlinearly coupled through charge conservation and reaction kinetics [17, 18], given by:

$$\nabla \cdot \vec{j}_e = -\nabla \cdot \vec{j}_l = -sj, \quad (2a)$$

$$j = j_0 \left[ \exp \left( \frac{(1-\alpha)F\eta}{RT} \right) - \exp \left( -\frac{\alpha F\eta}{RT} \right) \right], \quad (2b)$$

$$\eta = \phi_e - \phi_l - E_{eq}. \quad (2c)$$

The descriptions to the symbols in **Eqs. (1a)–(1b)** and **Eqs. (2a)–(2c)** are summarized in **Table 1**. Notably, the right-hand sides of **Eqs. (1a)** and **(1b)** have opposite signs, canceling each other when summed. Moreover, they exhibit a trigonometric hyperbolic dependence on the pair  $(\phi_e, \phi_l)$ , or more precisely, on their difference  $\phi_e - \phi_l$ . Furthermore, the current density  $j$  is negative for the reduction process and positive for the oxidation process.

Although it has not typically been framed this way in the relevant literature, **Eqs. (1a)–(1b)** and **Eqs. (2a)–(2c)** describe a system that aligns with the so-called dual-continuum approach in macroscopic modeling [19, 20]. This approach assumes that the two coupled dynamics are spatially superimposed, with their interaction governed by a pair of antisymmetric source/sink terms that enforce global conservation. By abstracting the system in this way, the dual-continuum approach effectively alleviates the need to resolve local porous geometry, significantly improving computational efficiency. This modeling strategy, along with its generalized versions, has been extensively studied in the porous media flow community as part of multiscale frameworks designed to upscale the coexistence of fast and slow fluid flow dynamics in complex media with well-distributed high- and low-conductivity regions [21, 22, 23, 24, 25].

In the context of porous electrodes, the dual-continuum setup considers the solid electrode and liquid electrolyte phases as coexisting everywhere and geometrically superimposed, such that  $\Omega_e = \Omega_l$ . The

**Table 1: Description of symbols in Eqs. (1a)–(1b) and Eqs. (2a)–(2c)**

Symbol	Description	Unit
<i>Primary unknowns:</i>		
$\phi_e$	Porous electrode potential	V
$\phi_l$	Electrolyte potential	V
<i>Secondary unknowns:</i>		
$\vec{j}_e$	Current density in the porous electrode	A/m <sup>2</sup>
$\vec{j}_l$	Current density in the electrolyte	A/m <sup>2</sup>
$j$	Reaction current density	A/m <sup>2</sup>
$\eta$	Overpotential	V
<i>Parameters:</i>		
$\sigma$	Electrical conductivity of the porous electrode	S/m
$\kappa$	Ionic conductivity of the electrolyte	S/m
$\alpha$	Electron transfer coefficient	-
$s$	Specific surface area of the porous electrode	m <sup>-1</sup>
$j_0$	Exchange current density	A/m <sup>2</sup>
$F$	Faraday constant, 96485	C/mol
$R$	Ideal gas constant, 8.314	J/(mol · K)
$T$	Operating temperature	K
$E_{eq}$	Equilibrium potential	V
$\Omega_e$	The modeling domain of electrode	-
$\Omega_l$	The modeling domain of electrolyte	-

porous electrode system exhibits two distinct conductivity regimes in the sense that the solid phase has significantly higher electrical conductivity than the electrolyte phase. The right-hand sides of **Eqs. (1a)** and **(1b)** form an antisymmetric pair, which can also be interpreted as internal or implicit boundary (interfacial) conditions governing the interaction between electrode and electrolyte dynamics. This coupling is generally described by the phenomenological Butler-Volmer equation [17, 18, 26], such as **Eq. (2b)**, along with some forms of correction for surface species concentrations [27, 28]. Unlike the porous media fluid flow applications, where such interfacial conditions are often approximated as pseudo-steady [21, 22, 23, 24, 25], the electrochemical system exhibits strong nonlinearity, following a hyperbolic semi-sinh dependence.

The numerical solution of **Eqs. (1a)** and **(1b)** presents challenges primarily in two aspects. First, the right-hand side is highly nonlinear, exhibiting a hyperbolic dependence on the unknowns ( $\phi_e$  and  $\phi_l$ ). Even a small variation in  $(\phi_e - \phi_l)$  can lead to significant changes in the right-hand side, potentially causing numerical instability. Second, a major challenge arises from the boundary conditions, which are intricate due to the coupled nature of the system and are dictated by the operating mode of the electrochemical cell. Electrochemical cells are typically operated under either *galvanostatic* or *potentiostatic* control, with *galvanostatic* operation being more common [11, 2]. Each mode determines the boundary conditions used in modeling. In *galvanostatic* operation, the current flux through the cell is fixed and externally controlled, allowing the potential to adjust dynamically in response to internal electrochemical reactions and mass transport. This applied current flux leads to an all-

Neumann boundary setup for the two Poisson equations, rendering the system under-constrained and making standard numerical solution strategies unsuitable due to singularity issues. In contrast, under *potentiostatic* operation, the potential difference between the electrodes (typically between the working and reference electrodes) is maintained at a prescribed value, while the current adapts accordingly to accommodate reaction kinetics and transport processes. This results in a Dirichlet boundary condition for the electrode potential, providing a much more well-posed setup for numerical solutions.

Most existing literature on continuum modeling of porous electrodes relies on commercial software such as COMSOL Multiphysics to solve the coupled system [15, 29, 30, 31, 32, 33, 14]. These studies typically describe the governing equations and galvanostatic boundary conditions (which are all-Neumann) before presenting simulation results obtained from COMSOL under homogeneous conductivity fields. However, they provide little insight into the underlying numerical schemes. According to COMSOL documentation [34], the galvanostatic total current condition “implies setting the potential of a boundary to be equal to an additional extra global potential degree of freedom (floating potential) to comply with the specified current condition.” Beyond this brief statement, no further technical details are available, making it unclear how the condition is enforced numerically. This lack of transparency significantly limits the generalizability of these studies, as the methodology cannot be extended to more complex, heterogeneous settings or adapted to different numerical frameworks. Moreover, since COMSOL’s numerical scheme is proprietary and non-adjustable, researchers have no control over the computational approach, making it impossible to evaluate its accuracy or explore alternative formulations. To the best of our knowledge, no existing literature discusses the numerical methods required to obtain the solutions, especially for the galvanostatic case. This gap motivates this work, aiming to provide such information and encourage researchers to develop and benchmark alternative numerical methods beyond those available in commercial solvers.

The main contributions of this paper are as follows: (1) We mathematically prove that, under galvanostatic conditions, **Eqs. (1a)** and **(1b)** admit a unique solution in terms of  $(\phi_e - \phi_l)$  and a unique pair of  $(\phi_e, \phi_l)$ , up to a shared constant shift in the solution space of  $\phi_e$  and  $\phi_l$ . (2) We provide two methods to eliminate this constant shift: one is a Lagrange constraint formulation derived using a unified energy functional of the two coupled Poisson equations, and the other is a Dirichlet boundary substitution approach based on Gauss’s theorem. (3) We develop two nonlinear solution schemes for solving the galvanostatic problem: a decoupled approach and a fully coupled approach. (4) We demonstrate that, without introducing any additional reference potential, a solution can still be obtained using global constraining in a purely mathematical sense to address the singular system in the fully coupled scheme. (5) We provide a code implementation capable of solving both 2D homogeneous and heterogeneous conductivity cases, allowing for the reproduction of the results presented in this paper and can seed further development.

The remainder of this paper is structured as follows. In **Section 2**, we provide a brief recap of the underlying mathematical model. **Section 3** and **Section 4** detail the numerical approaches developed to solve this class of problems. Validation and analysis examples are presented in **Section 5**, followed by conclusions in **Section 6**.

## 2 Mathematical Model

### 2.1 Governing Equations

To simplify the coupled nonlinear Poisson problem without loss of generality, we consider a symmetric redox reaction involving a single-electron transfer. Under the assumption of a symmetric energy barrier, the electron transfer coefficient is taken as  $\alpha = 0.5$ , following the conventional treatment in classical electrochemical kinetics [11, 35]. Additionally, we focus on the reduction process, where the reaction current density  $j$  is negative, consistent with the convention that electron transfer into the electrode corresponds to reduction [2]. This typically represents either the charging cycle on the negative electrode or the discharging cycle in the positive counterpart.

**Note:** These simplifications are made for clarity and conciseness in presenting the numerical methods. The solution strategies introduced in **Sections 3** and **4** remain broadly applicable to oxidation processes, systems with asymmetric electron transfer coefficients, and cases involving transient dynamics such as species transport via diffusion, convection, and migration.

After those simplifications, **Eq. (1a) - (2c)** can be reduced to:

$$\nabla \cdot (-\sigma \nabla \phi_e) = -a \sinh(b\eta) \quad \text{in } \Omega_e, \quad (3a)$$

$$\nabla \cdot (-\kappa \nabla \phi_l) = a \sinh(b\eta) \quad \text{in } \Omega_l, \quad (3b)$$

where  $\eta := \phi_e - \phi_l - E_{eq}$ ,  $a = 2sj_0$ , and  $b = \frac{0.5F}{RT}$ . The Butler-Volmer equation (**Eq. (2b)**) is rewritten as a sinh function because  $\alpha = 0.5$ .

### 2.2 Model Geometry

The model geometry considered in this paper is illustrated in **Figure 1**. The domain representing a half-cell setup comprises a porous electrode positioned between a current collector on the left and a membrane separator on the right. The porous electrode is modeled as a composite material comprising a solid matrix (shown in gray) and pore spaces (shown in white), the latter being filled with electrolyte.

The model extends over a width  $W$  in the  $x$ -direction and a height  $H$  in the  $y$ -direction, with the current collector and membrane separator defining the left and right boundaries, respectively. The entire system can be characterized by its dual-continuum nature, consisting of a solid electrode-continuum  $\Omega_e$  and a liquid-continuum  $\Omega_l$  that are spatially superimposed (i.e.,  $\Omega_e = \Omega_l$ ).

In the following, when we use the symbol  $\Omega$ , it denotes both the electrode and the electrolyte domains without explicitly distinguishing them. The redox reaction interface between these two continua is formed by the surface of the pore space. It acts as an implicit internal interfacial boundary where electrochemical reactions occur. This dual-continuum configuration serves as the foundation for describing the coupled potential fields arising from electronic and ionic conduction, which are numerically solved in the subsequent sections.

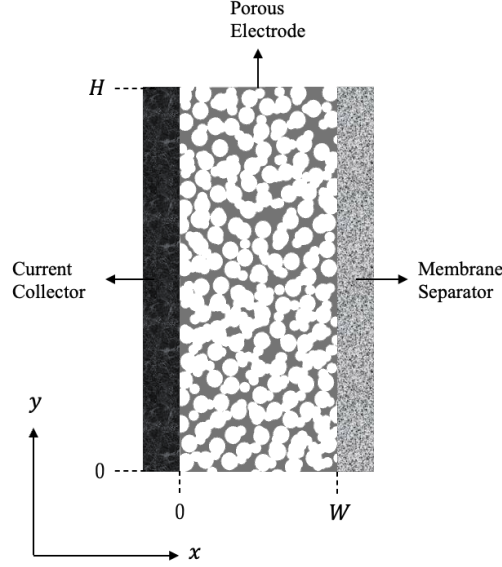


Figure 1: The half-cell porous electrode model geometry considered in this paper

## 2.3 Boundary Conditions

Boundary conditions are required at all boundaries for solving **Eqs. (3a) and (3b)**. Here, we consider both the galvanostatic and potentiostatic operating conditions. That is, we assume the boundaries consist entirely of either Dirichlet or Neumann conditions.

### 2.3.1 Galvanostatic

Under galvanostatic condition, the left boundary  $x = 0$  of  $\Omega_e$ , attaching to the current collector, is subjected to a fixed current density applied through the external circuit. Since the membrane separator is not conductive to electrons, the right boundary  $x = W$  of  $\Omega_e$  is considered to have no electron current flux. Additionally, the top and bottom boundaries are assumed to be insulated to current flux. The boundary conditions for the porous electrode domain are summarized as follows:

$$\sigma \frac{\partial \phi_e}{\partial n} = \begin{cases} -j_{\text{applied}}, & \text{at } x = 0, \\ 0, & \text{at } x = W, y = 0, y = H, \end{cases} \quad (4)$$

where  $j_{\text{applied}}$  is the applied current density ( $A/m^2$ ) and  $\frac{\partial \phi_e}{\partial n}$  denotes the directional derivative in the direction normal (pointing outwards) to the boundary.

For the electrolyte domain, its left boundary  $x = 0$  does not support ionic conduction, resulting in no ionic current flux. Conversely, at its right boundary  $x = W$  in contact with the membrane separator, there is supporting ionic flux between the positive and negative electrolyte regions. This ionic current flux balances the charge changes caused by electrochemical reactions and completes the internal current circuit. Under galvanostatic operation, the ionic current density at  $x = W$  matches

the current density applied to the electrode via the current collector. The top and bottom boundaries are insulated with respect to ionic flux. The boundary conditions for the electrolyte are thus expressed as:

$$\kappa \frac{\partial \phi_l}{\partial n} = \begin{cases} j_{\text{applied}}, & \text{at } x = W, \\ 0, & \text{at } x = 0, y = 0, y = H. \end{cases} \quad (5)$$

**Note:** In **Eqs. (4)** and **(5)**,  $j_{\text{applied}}$  represents a non-negative value, while in **Eq. (2b)**,  $j$  can be positive, negative, or zero, depending on the reaction conditions. Apparently, under galvanostatic condition, **Eqs. (3a)** and **(3b)** are subject to all-Neumann boundary conditions.

### 2.3.2 Potentiostatic

Under potentiostatic condition, the left boundary  $x = 0$  of  $\Omega_e$ , attaching to the current collector, is set to an externally specified potential as a Dirichlet boundary condition. The remaining boundaries are the same as the galvanostatic case. Thus, we have:

$$\begin{cases} \phi_e = V_{\text{applied}}, & \text{at } x = 0, \\ \sigma \frac{\partial \phi_e}{\partial n} = 0, & \text{at } x = W, y = 0, y = H. \end{cases} \quad (6)$$

For the electrolyte domain, the boundaries at  $x = 0$ ,  $y = 0$ , and  $y = H$  of  $\Omega_l$  remain under zero-flux conditions. However, the boundary at  $x = W$  is not explicitly specified by the operating condition. We can impose either Dirichlet or Neumann boundaries there and then numerically sweep the respective boundary values when solving the system. Thus, we consider two cases as in **Eqs. (7)** and **(8)**.

$$\begin{cases} \phi_l = V_{\text{sweep}}, & \text{at } x = W, \\ \kappa \frac{\partial \phi_l}{\partial n} = 0, & \text{at } x = 0, y = 0, y = H, \end{cases} \quad (7)$$

$$\kappa \frac{\partial \phi_l}{\partial n} = \begin{cases} j_{\text{sweep}}, & \text{at } x = W, \\ 0, & \text{at } x = 0, y = 0, y = H, \end{cases} \quad (8)$$

where  $V_{\text{sweep}}$  and  $j_{\text{sweep}}$  are to be swept during solution.

## 3 Numerical Methods: Galvanostatic Solution

We consider numerical solutions for the coupled nonlinear Poisson equations in **Eqs. (3a)** and **(3b)**, subject to the boundary conditions given in **Eqs. (4)** and **(5)**. Due to the nonlinear source and sink terms, iterative linearization techniques such as Newton–Raphson method are typically employed in both decoupled and fully coupled solution schemes.

However, the major challenge for galvanostatic solution arises from the all-Neumann boundary conditions, which constrain only the derivatives of the solution rather than their absolute values. This may lead to non-uniqueness in the respective solution spaces of  $\phi_e$  and  $\phi_l$ . Such a situation often results in a singular system matrix after discretization, complicating the numerical solution process. In this section, we provide decoupled and coupled numerical methods to address this challenge.

### 3.1 Solution Existence and Uniqueness

#### 3.1.1 Existence

For Poisson problems subject exclusively by Neumann boundary conditions, the existence of a solution requires satisfying a compatibility condition derived from Gauss's theorem. For **Eqs. (3a)** and **(3b)**, along with **Eqs. (4)** and **(5)**, **Eqs. (9a)** and **(9b)** must hold. In a physical sense, this requirement is equivalent to charge conservation.

$$\int_{\Omega_e} (-f) d\Omega_e = - \int_{\partial\Omega_e} \sigma \frac{\partial\phi_e}{\partial n} dS_e, \quad (9a)$$

$$\int_{\Omega_l} f d\Omega_l = - \int_{\partial\Omega_l} \kappa \frac{\partial\phi_l}{\partial n} dS_l, \quad (9b)$$

Here,  $f = a \sinh(b\eta)$ , while  $\Omega_{e/l}$  and  $\partial\Omega_{e/l}$  represent the interior and boundary of the model domain  $\bar{\Omega}_{e/l}$ , respectively. Additionally,  $dS_{e/l}$  denotes a differential surface element on  $\partial\Omega_{e/l}$ .

#### 3.1.2 Uniqueness

It is known that a solution to a Neumann Poisson problem can only be unique up to an additive constant, assuming the solution compatibility condition is met. Here, for this nonlinearly coupled Neumann Poisson system, we prove that the system admits a unique set of solution pairs  $(\phi_e, \phi_l)$  up to **an additive constant** (see **Appendix A**). That is, the class of solution pairs can be characterized by

$$\{(\phi_e, \phi_l) \mid \phi_e = \phi_e^* + C, \quad \phi_l = \phi_l^* + C, \quad C \in \mathbb{R}\} \quad (10)$$

where  $(\phi_e^*, \phi_l^*)$  is any pair of particular solution to **Eqs. (3a)** and **(3b)** subject to the all Neumann boundary conditions in **Eqs. (4)** and **(5)**.

**Eq. (10)**

- shows that the system admits a unique solution in terms of  $(\phi_e - \phi_l)$ , where

$$\phi_e - \phi_l = \phi_e^* - \phi_l^*; \quad (11)$$

- explains why the galvanostatic solution is challenging, as  $\phi_e$  and  $\phi_l$  can freely shift in their respective solution spaces, complicating numerical solution strategies;



- suggests such shifts are subject to a shared constant across the two equations for  $\phi_e$  and  $\phi_l$ . Consequently, if we impose any pre-specified constant value on either  $\phi_e$  or  $\phi_l$ , we can eliminate the extra degree of freedom, making the numerical solution feasible.

Therefore, **Eq. (10) implies that, when solving the system numerically,  $\phi_e$  is internally referenced to  $\phi_l$  over the domain, and vice versa. Additionally, the system requires **one extra reference value** to eliminate the arbitrary constant shift in  $\phi_e$  and  $\phi_l$ .** Then, the task becomes imposing such referencing mechanisms in the numerical strategy to uniquely determine the galvanostatic solution.

Adding a reference point to the system should be straightforward, as we can arbitrarily select a location ( $x^*$ ) within the domain and impose  $\phi_e(x^*)$  or  $\phi_l(x^*)$  as an arbitrary constant. In the specific context of an electrode system, it is natural to assume that some point within the electrode is grounded, meaning the potential at this point is zero. This grounded point can then serve as the reference for both equations. A more physically meaningful choice is to assume that the current collector is grounded. Consequently, at the electrode boundary attached to the current collector, or in a region very close to this boundary, we let the potential be zero.

However, the internally referencing between the numerical solutions  $\phi_e$  and  $\phi_l$  may depend on the chosen approach for solving the two nonlinear Poisson equations. Next, we present two approaches to enforce a fixed-location constant potential reference. Then, we provide the complete numerical approaches to solve the coupled system using decoupled and fully coupled schemes.

## 3.2 Constant Potential Referencing

### 3.2.1 Lagrange Constraint Method (LCM)

To retain the original all-Neumann boundary conditions and governing Poisson equations, we employ the Lagrange multiplier method to enforce a constant potential constraint in  $\Omega_e$ . This constraint serves as the reference potential for the coupled system. While the location and value of this reference can be arbitrary, in this work, we select a location near the left boundary of  $\Omega_e$  and set the potential to zero, as this choice is physically motivated.

Since the problem involves two coupled Poisson equations, we derive the following Lagrange multiplier formulation using a unified energy functional of the coupled system (See **Appendix B**), with Neumann conditions given in **Eqs. (4)–(5)**:

$$\nabla \cdot (-\sigma \nabla \phi_e) + f + \sum_{i=1}^m \lambda_i \delta(x - x_i) = 0 \quad \text{in } \Omega_e, \quad (12a)$$

$$\nabla \cdot (-\kappa \nabla \phi_l) - f = 0 \quad \text{in } \Omega_l, \quad (12b)$$

$$\phi_e(x_i) - c_i = 0 \quad \text{for } i = 1, 2, \dots, m. \quad (12c)$$

Here,  $\delta(x - x_i)$  is the Dirac delta function at  $x_i \in \Omega_e$ , enforcing the constraint at  $\Gamma_1 := \{x_1, x_2, \dots, x_m\}$ . The set  $\Lambda_e := \{\lambda_i \mid i = 1, 2, \dots, m\}$  represents the corresponding Lagrange multipliers. In other words,

the values of  $\phi_e$  at  $x_i$  are constrained to a constant  $c_i$ , serving as the reference potential for the system. A similar formulation can be derived for the electrolyte equation if a fixed-location reference is applied to it.

**Note:** In addition to Lagrange multipliers, other methods exist for imposing local constraints in  $\Omega$ , such as the penalty method [36] and direct matrix modification [37]. The penalty method uses a penalty term that approximates the constraint, requiring a large penalty coefficient to enforce it strictly. This coefficient is typically selected heuristically or based on experience, and often lacks theoretical justification. This may lead to numerical instability and convergence issues. Direct matrix modification enforces the constraint by modifying the matrix. For instance, if a finite volume or a controlled-volume finite difference discretization is adopted, the row of the resulting linear system corresponding to the constrained cell is modified by setting the diagonal entry to 1, zeroing out all off-diagonal entries of the matrix, and replacing the right-hand side with the constraint value  $C$ . While this method forces the constrained solution to equal  $C$  exactly, it deletes the local governing Poisson equation at the constraint location, potentially disrupting the neighboring flux balance and conservation laws. In contrast, the Lagrange multiplier approach is theoretically rigorous, enforcing the exact constraint without approximation errors and preserving the original PDE structure (see **Appendix B**). However, it can increase system size, leading to additional computational complexity and potential scaling issues.

### 3.2.2 Dirichlet Substitution Method (DSM)

Recall **Section 3.1.1**. Gauss's theorem reveals an intrinsic property of Poisson equations that holds regardless of the specific boundary conditions (Dirichlet or Neumann) explicitly prescribed. Specifically, the integral of the boundary fluxes over  $\partial\Omega$  must balance the integral of the source/sink  $f$  over  $\Omega$ . This implies that even when Dirichlet boundary conditions are imposed without explicitly specifying the corresponding boundaries' fluxes, their underlying flux contributions at those boundaries still must satisfy the global compatibility condition, or charge conservation, together with other Neumann boundaries that may be present.

As a result, in the all-Neumann setup, we can substitute one of the boundaries with an arbitrary Dirichlet condition (i.e. a potential value) without altering the original coupled system. This Dirichlet condition is then act as the reference potential for the system.

For instance, if we replace the original Neumann condition on the electrode domain at  $x = 0$  with an arbitrary Dirichlet condition ( $\phi_e|_{x=0} = \phi_{\text{ref}}$ ), the underlying flux across this boundary remains unchanged, as shown in **Eqs. (13)**, **(9a)** and **(9b)**. Note: the boundary fluxes on  $\Omega_e$  at  $x = W$ ,  $y = 0$ , and  $y = H$ , as well as those on  $\Omega_l$  at  $x = 0$ ,  $y = 0$ , and  $y = H$ , are all zero, according to **Eqs. (4)** and **(5)**. The subscripts  $\mathcal{N}$  and  $\mathcal{D}$  refer to the specified Neumann and Dirichlet boundaries of the domain, respectively.

$$\int_{\partial\Omega_{e,\mathcal{D}}|_{x=0}} \sigma \frac{\partial\phi_e}{\partial n} dS_e = - \int_{\Omega_e} (-f) d\Omega_e = \int_{\Omega_l} f d\Omega_l = - \int_{\partial\Omega_{l,\mathcal{D}}|_{x=W}} \kappa \frac{\partial\phi_l}{\partial n} dS_l \quad (13)$$

### 3.3 Nonlinear Solution Schemes

As mentioned in **Section 3.1**, in addition to imposing a constant reference potential, it is essential to establish internal referencing between  $\phi_e$  and  $\phi_l$  during the nonlinear solution process, which depends on the numerical schemes used to solve the coupled system. We consider both decoupled schemes, where the two equations are solved sequentially, and fully coupled schemes, where they are solved simultaneously.

#### 3.3.1 Decoupled Scheme

We use a staggered decoupling scheme for the coupled system **Eqs. (3a) and (3b)**. At iteration  $k+1$ , the variables  $\phi_e$  and  $\phi_l$  are updated sequentially, each using the most recent value available from the other domain at iteration  $k$ . This reformulates the coupled problem into a sequence of independent problems. **Table 2** outlines the basic procedures. As shown in **Eqs. (14a) and (14b)**, when  $m = k$ , it corresponds to a fully explicit scheme, whereas  $m = k+1$  indicates the need for an implicit solve. We choose  $m = k+1$  since an explicit scheme can be unstable for this type of elliptic PDE.

**Table 2: Steps of decoupled scheme for solving Eqs. (3a)–(3b)**

Step	Description
<i>Initialization</i>	Set the initial guess for the nonlinear term $f^0(\eta)$ using average local current density.
<i>Iteration</i>	<ol style="list-style-type: none"> <li>Solve the following two Poisson equations sequentially:                             <math display="block">\nabla \cdot (-\sigma \nabla \phi_e^{k+1}) = -f(\phi_e^m - \phi_l^k - E_{\text{eq}}), \quad (14a)</math> <math display="block">\nabla \cdot (-\kappa \nabla \phi_l^{k+1}) = f(\phi_e^k - \phi_l^m - E_{\text{eq}}). \quad (14b)</math> <p>subject to boundary conditions <b>(4)</b> and <b>(5)</b>. <math>k</math> is the iteration index.</p> </li> <li>Update the nonlinear term to <math>f^{k+1} := f(\eta^{k+1})</math> for convergence check letting <math>\eta^{k+1} = \phi_e^{k+1} - \phi_l^{k+1} - E_{\text{eq}}</math>.</li> <li>Check convergence: If <math>\ f^{k+1} - f^k\ </math> falls below a predefined threshold, proceed to output. Otherwise, continue the update.</li> </ol>
<i>Output</i>	Return the converged $\phi_e$ and $\phi_l$ .

The stopping criterion is chosen to reflect the strong sensitivity of the sinh function to changes in  $\eta$ , which helps monitor convergence effectively and ensures the stability of the iterative scheme. This decoupling introduces two main issues:

- The coupling between  $\phi_e$  and  $\phi_l$  is weakly impeded through the right-hand side  $f$ , as there is no explicit gridblock-wise referencing between  $\phi_e$  and  $\phi_l$  in this sequential solution strategy.
- Imposing a constant reference potential to  $\Omega_e$  resolves the singularity of **Eq. (14a)**. However, **Eq. (14b)** remains singular.

To address these two issues, we introduce an additional constant reference  $c_l$  potential to  $\Omega_l$ . Our motivation for this choice is twofold: first, to resolve the singular system matrix in **Eq. (14b)**; second, to provide a mechanism that enables  $\phi_e$  and  $\phi_l$  to cross-reference within a sequential solution scheme.

**Note:** According to **Eq. (10)**, the system requires only a single constant of reference potential to isolate a unique pair of solutions for  $(\phi_e, \phi_l)$ . This implies that any additional reference potential cannot be arbitrarily assigned, as a zero reference potential has already been imposed in  $\Omega_e$ . Consequently,  $c_l$  must be treated as an unknown and requires a closure condition to be determined self-consistently. A natural choice for such a condition is the compatibility constraint or charge conservation, as given in **Eqs. (9a)** and **(9b)**. To determine the appropriate value of  $c_l$ , a search algorithm can be employed. Thus, we then show both **LCM** and **DSM** can be adapted to iteratively find a  $c_l$  to satisfy the system dynamics.

**LCM Discretization.** We begin with the discretized form of **Eqs. (12a) – (12c)**, which reads

$$A_e \Phi_e + \Delta_e^T \Lambda_e = F_e, \quad (15a)$$

$$\Delta_e \Phi_e = C_e, \quad (15b)$$

where  $A_e$  is the system matrix,  $F_e$  is the discretized right-hand side vector,  $\Phi_e := [\phi_1^{k+1}, \phi_2^{k+1}, \dots]^T$ ,  $\Lambda_e$  is the Lagrange multiplier vector, and  $C_e := c_e \mathbf{1}_{n_c}$  is the reference potential vector, where  $\mathbf{1}_{n_c} = [1, 1, \dots, 1]^T \in \mathbb{R}^{n_c}$  and  $n_c$  is the number of constrained gridblocks. The Neumann boundary condition information is incorporated  $A_e$  and  $F_e$ .  $\Delta_e$  is a Dirac delta matrix with entries of 1 at the locations corresponding to the constraints, and 0 elsewhere. It projects the  $\Lambda_e$  and  $\Phi_e$  vectors onto the indices of the constrained gridblocks. The matrix  $\Delta_e$  has dimensions  $n_c \times N$ , where  $N$  is the total number of gridblocks. Each row of this sparse matrix corresponds to a constrained gridblocks, featuring a single 1 at the global index of that grid and 0 in all other positions. The corresponding discretization of  $\Omega_l$  can be done in an analogous way. The resulting linear systems are:

$$\begin{bmatrix} A_e & \Delta_e^T \\ \Delta_e & 0 \end{bmatrix} \begin{bmatrix} \Phi_e \\ \Lambda_e \end{bmatrix}^{k+1} = \begin{bmatrix} F_e^{k/k+1} \\ C_e \end{bmatrix}, \quad (16a)$$

$$\begin{bmatrix} A_l & \Delta_l^T \\ \Delta_l & 0 \end{bmatrix} \begin{bmatrix} \Phi_l \\ \Lambda_l \end{bmatrix}^{k+1} = \begin{bmatrix} F_l^{k/k+1} \\ C_l^* \end{bmatrix}. \quad (16b)$$

where  $C_l^* := c_l^* \mathbf{1}_{n_l}$  is a vector parametrized by an unknown  $c_l^*$ . The superscript  $k/k+1$  indicates, for example,  $F_e$  is evaluated using  $\phi_e^{k/k+1}$ .

**DSM Discretization.** For **DSM**, the discretization is simpler as  $c_e$  and  $c_l^*$  are imposed as constant Dirichlet boundaries at  $x = 0$  and  $x = W$ . The resulting discretized system is given by:

$$A_e \Phi_e^{k+1} = F_e^{k/k+1} \quad \text{and} \quad A_l \Phi_l^{k+1} = F_l^{k/k+1} \quad (17)$$

where the corresponding Dirichlet boundaries are incorporated in  $(A_e, F_e)$  and  $(A_l, F_l)$ .

**Unknown Reference Potential Search.** We determine the unknown reference potential  $c_l^*$  by formulating an optimization problem to isolate its unique value that satisfies **Eqs. (9a) and (9b)**. Together with **Eq. (13)**, we define the following objective function regarding  $c_l^*$ :

$$c_l^* = \arg \min_{c_l} \left\| \int_{\mathcal{B}} j_{\text{applied}} dS + \int_{\Omega} f(\cdot; c_l) d\Omega \right\|^2, \quad \mathcal{B} = \partial\Omega|_{x=0} \text{ or } \mathcal{B} = \partial\Omega|_{x=W}. \quad (18)$$

To solve this optimization problem, we employ a gradient descent approach with a line search mechanism [38] that dynamically adjusts the search step size (see **Appendix C**). This method iteratively refines the reference potential with linear convergence.

In **Table 3**, we outline the complete solution strategy. It incorporates the staggered iteration as an inner loop for solving the nonlinear Poisson equations sequentially, with either the LCM or DSM approach used to impose  $c_e$  and  $c_l^*$ . The combination of the outer search loop and the inner Picard iteration thus provides a numerical framework for obtaining galvanostatic solutions in a decoupled fashion while ensuring internal referencing between  $\phi_e$  and  $\phi_l$ . This approach can address the singularity issues and enforces charge conservation in a self-consistent manner.

**Table 3: The galvanostatic solution algorithm using decoupled scheme**

Step	Description
<i>Initialization</i>	Set a initial reference potential $c_l^*$ .
<i>Solve</i>	Refer to <b>Table 2</b> . Use <b>LCM</b> or <b>DSM</b> to solve the coupled nonlinear Poisson equations in a sequential fashion. Iterate until convergence or reaching stopping criteria.
<i>Optimization</i>	<ol style="list-style-type: none"> <li>1. Check convergence (<b>Eq. (18)</b>): If the mismatch is below the prescribed tolerance, exit and output the solution <math>\phi_e</math> and <math>\phi_l</math>; otherwise, continue.</li> <li>2. Compute the gradient of <b>Eq. (18)</b>.</li> <li>3. Perform line search to obtain an optimized step size.</li> <li>4. Update <math>c_l^*</math> and rerun to solve the decoupled PDEs.</li> </ol>
<i>Output</i>	Return the globally converged solution $\phi_e$ and $\phi_l$ .

### 3.3.2 Fully Coupled Scheme

If we can construct a coupled system matrix where  $\phi_e$  and  $\phi_l$  are cross-referenced to each other gridblock-wise, the need for introducing  $c_l^*$  may be alleviated. This motivates us to explore a fully coupled scheme that can solve the two nonlinear Poisson equations (**Eqs. (3a)–(3b)**) simultaneously. This is achieved by deriving the corresponding coupled Newton-Raphson system, which solves for  $\phi_e$  and  $\phi_l$  using a fully coupled Jacobian matrix. Unlike the decoupled scheme, where  $\phi_l$  is fixed while solving  $\phi_e$  or vice versa, here, both are treated fully implicitly. As shown below, the fully coupled Jacobian matrix captures the cross-dependencies between the two potential fields, preventing any arbitrary shifts in their values and naturally enforcing internal referencing without requiring an additional search for  $c_l^*$ .

We provide implementations for both the **LCM** and **DSM** approaches to impose a constant reference potential in the system for the coupled scheme. Additionally, we provide a global constraining method that resolves the singular system by first computing the unique  $\phi_e - \phi_l$ , and then recovering  $\phi_e$  and  $\phi_l$  through post-processing under an arbitrary constant reference potential.

**LCM Discretization.** We start with the discretized form of **Eqs. (12a)–(12c)**, which is given as:

$$Q_e^L = A_e \Phi_e - F_e + \Delta_e^T \Lambda_e, \quad (19a)$$

$$Q_l^L = A_l \Phi_l - F_l, \quad (19b)$$

$$G_e^L = \Delta_e \Phi_e - C_e. \quad (19c)$$

where  $F_e$  and  $F_l$  are the discretized forms of  $-f$  and  $f$ , respectively, and the superscript  $L$  denotes Lagrange. Then, the residual can be written in the following compact way:

$$R^L = [Q_e^L, Q_l^L, G_e^L]^T \quad (20)$$

The corresponding extended Jacobian matrix thus is:

$$J^L = \frac{\partial R^L}{\partial U^L}, \quad U^L = [\Phi_e, \Phi_l, \Lambda_e]^T \quad (21)$$

Then, the extended Jacobian system is:

$$J^L \tau_U^L = -R^L \quad (22)$$

The nonlinear update step is carried out iteratively via:

$$U^{L,k+1} = U^{L,k} + \tau_U^L = U^{L,k} - \frac{R^{L,k}}{J^{L,k}} \quad (23)$$

where  $k$  is the Newton-Raphson iteration index and  $\tau_U^L$  is the update. The elements of the  $J^L$  is given by:

$$\begin{aligned} \frac{\partial Q_e^L}{\partial \Phi_e} &= A_e - \frac{\partial F_e}{\partial \Phi_e}, & \frac{\partial Q_e^L}{\partial \Phi_l} &= -\frac{\partial F_e}{\partial \Phi_l}, \\ \frac{\partial Q_l^L}{\partial \Phi_l} &= A_l - \frac{\partial F_l}{\partial \Phi_l}, & \frac{\partial Q_l^L}{\partial \Phi_e} &= -\frac{\partial F_l}{\partial \Phi_e}, \\ \frac{\partial Q_e^L}{\partial \Lambda_e} &= \Delta_e^T, & \frac{\partial G_e^L}{\partial \Phi_e} &= \Delta_e. \end{aligned} \quad (24)$$

Then, the matrix form of the extended Jacobian system is:

$$\begin{bmatrix} A_e - \frac{\partial F_e}{\partial \Phi_e} & -\frac{\partial F_e}{\partial \Phi_l} & \Delta_e^T \\ -\frac{\partial F_l}{\partial \Phi_e} & A_l - \frac{\partial F_l}{\partial \Phi_l} & 0 \\ \Delta_e & 0 & 0 \end{bmatrix} \begin{bmatrix} \tau_{\Phi_e} \\ \tau_{\Phi_l} \\ \tau_{\Lambda_e} \end{bmatrix} = \begin{bmatrix} Q_e^L \\ Q_l^L \\ G_e^{L,r} \end{bmatrix}. \quad (25)$$

where the superscript  $r$  denotes that it contains the constant reference potential. **Note:**  $J^L$  is well-posed, and the terms  $[-\frac{\partial F_e}{\partial \Phi_l}]$  and  $[-\frac{\partial F_l}{\partial \Phi_e}]$  enforce the cross-referencing between  $\phi_e$  and  $\phi_l$ . As a result, solving **Eq. (25)** iteratively yields a unique pair of solutions for  $\phi_e$  and  $\phi_l$ .

**Remark 3.1.** *Since the nonzero entries of  $\Delta_e$  are 1,  $J^L$  tends to be poorly scaled, which may lead to numerical issues. For this type of extended Lagrange system, naive global rescaling may not work. It is recommended to perform decomposed scaling of the Lagrange components to bring them to a similar magnitude as the non-Lagrange part, and then reassemble to a rescaled extended Jacobian system. By doing so, the numerical instability caused by poor scaling should be mitigated.*

**DSM Discretization.** The Jacobian system of DSM can be readily obtained by removing the Lagrange components and applying appropriate modifications to  $A_e$  and  $A_l$ , as well as  $[Q_e]$  and  $[Q_l]$ , to accommodate the Dirichlet boundary conditions. The resulting Jacobian system is:

$$\begin{bmatrix} A_e^d - \frac{\partial F_e}{\partial \Phi_e} & -\frac{\partial F_e}{\partial \Phi_l} \\ -\frac{\partial F_l}{\partial \Phi_e} & A_l - \frac{\partial F_l}{\partial \Phi_l} \end{bmatrix} \begin{bmatrix} \tau_{\Phi_e} \\ \tau_{\Phi_l} \end{bmatrix} = \begin{bmatrix} Q_e^{d,r} \\ Q_l \end{bmatrix}. \quad (26)$$

where the subscript  $d$  denotes the incorporation of Dirichlet boundary substitutions, and the superscript  $r$  indicates the inclusion of the constant reference potential.

**Global Constraining Method (GCM).** Recall **Eqs. (10)** and **(11)**. Even if we allow a shared constant shift in  $\phi_e$  and  $\phi_l$  during the solution process, their difference,  $\phi_e - \phi_l$ , remains unique. This implies that if the two potentials are cross-referenced with each other gridblock-wise during Newton-Raphson, the original Jacobian system (assembled using all-Neumann boundary conditions as in **Eq. (27)**) may be sufficient to guarantee that the system admits a unique solution in terms of  $\phi_e - \phi_l$ . Thus, the task reduces to finding an appropriate method to solve the singular system. We can introduce some global constraints using mathematically meaningful measures to ensure that the singular system is solvable in a stable manner. Here, we provide three of such global constraining measures:

- $\min_{\tau_{\Phi}} \|\tau_{\Phi}\|^2$  subject to **Eq. (27)**, which selects the smallest possible magnitude of  $\tau_{\Phi}$  in a least-squares sense, ensuring that the free shared constant shift is eliminated [39];
- $\min_{\tau_{\Phi}} \|J \tau_{\Phi} - Q\|^2$  subject to **Eq. (27)**, which ensures that the computed solution is as close as possible to satisfying  $J \tau_{\Phi} = Q$ , by restricting the solution search space to a Krylov subspace [40];
- $\min_{\tau_{\Phi}} \|J \tau_{\Phi} - Q\|^2 + \lambda_T \|I \tau_{\Phi}\|^2$  subject to **Eq. (27)**, which applies Tikhonov regularization [41] to balance the trade-off between minimizing the least-squares residual of  $J \tau_{\Phi} = Q$  and controlling

the magnitude of  $\tau_\Phi$ . The regularization term  $\lambda_T \|I\tau_\Phi\|^2$  penalizes large values of  $\tau_\Phi$ , improving numerical stability and mitigating the effects of ill-conditioning in  $J$ . The parameter  $\lambda_T$  determines the weight of the regularization, with larger values enforcing stronger damping on  $\tau_\Phi$ .

where  $\tau_\Phi = [\tau_{\Phi_e}, \tau_{\Phi_l}]^T$  and  $Q = [Q_e, Q_l]^T$ . In implementation, we can use the Moore–Penrose pseudoinverse [42], which minimizes  $\|\tau_\Phi\|^2$ . We may also apply MINRES (Minimum Residual Method) to minimize  $\|J\tau_\Phi - Q\|^2$  [43]. Alternatively, Tikhonov regularization can be used with a least-squares solver [44, 45] to minimize  $\|J\tau_\Phi - Q\|^2 + \lambda_T \|I\tau_\Phi\|^2$ . We refer to this approach as LSTR (Least-Squares with Tikhonov Regularization).

$$\begin{bmatrix} A_e - \frac{\partial F_e}{\partial \Phi_e} & -\frac{\partial F_e}{\partial \Phi_l} \\ -\frac{\partial F_l}{\partial \Phi_e} & A_l - \frac{\partial F_l}{\partial \Phi_l} \end{bmatrix} \begin{bmatrix} \tau_{\Phi_e} \\ \tau_{\Phi_l} \end{bmatrix} = \begin{bmatrix} Q_e \\ Q_l \end{bmatrix}. \quad (27)$$

Once we obtain a particular pair  $(\phi_e^*, \phi_l^*)$ , the post-processing step to compute the corresponding  $(\phi_e, \phi_l)$  under a given constant reference potential  $C$  is straightforward. Suppose the system is referenced at location  $x_0$  with  $\phi_e(x_0) = C$ , we can determine the shift as  $\phi_e^*(x_0) - C$ . The final solution pair under this constant reference potential is then computed as:

$$(\phi_e, \phi_l) = (\phi_e^*, \phi_l^*) - [\phi_e^*(x_0) - C]. \quad (28)$$

**Remark 3.2.** *In comparison to the decoupled Picard-based approach, the fully coupled solution strategy is more attractive due to its inherent cross-referencing between  $\phi_e$  and  $\phi_l$ , which eliminates the need to impose an additional unknown constant reference. However, the fully coupled approach introduces additional implementation and computational costs, including the need to construct the Jacobian system and solve a larger system—twice the size of each sequential solve in the decoupled Picard iteration. In the decoupled approach, this reference must be determined through an extra outer search loop, requiring multiple iterations of solving the two equations and potentially necessitating fine-tuning of search hyperparameters.*

## 4 Numerical Methods: Potentiostatic Solution

For the sake of completeness, we briefly outline the numerical strategy for solving the potentiostatic system. In comparison with the galvanostatic condition, the potentiostatic solution is more straightforward, as the coupled system includes a fixed Dirichlet boundary condition for  $\Omega_e$  at  $x = 0$  (**Eq. 6**). Unlike the galvanostatic case, where boundary conditions of  $\Omega_l$  are explicitly specified at  $x = 0$  and  $x = W$ , the boundary condition of  $\Omega_l$  at  $x = W$  in the potentiostatic system is not directly prescribed. Therefore, we consider two possible cases, as defined by **Eqs. (7) and (8)**: Dirichlet at  $x = W$  and Neumann at  $x = W$ . However, the system admits multiple solutions depending on the specific assigned boundary values at  $x = W$  for  $\Omega_l$ , whether Dirichlet or Neumann. We thus can numerically sweep such boundary values to compute a series of different potentiostatic responses for both cases.



**Dirichlet at  $x = W$ .** This case is trivial as the coupled system is well-constrained without any solution ambiguity. We can solve the system using either decoupled or fully-coupled approaches by sweeping the value  $V_{\text{sweep}} = \phi_l(x = W)$ , provided that the sweeping boundary value remains within a physically meaningful and compatible range. For instance, in a charging process at the negative electrode,  $V_{\text{sweep}}$  should be larger than  $V_{\text{applied}} = \phi_e(x = 0)$ .

**Neumann at  $x = W$ .** The  $\Omega_l$  setup in this case is analogous to the galvanostatic situation, where the system is subject to all-Neumann boundary conditions. Since  $\phi_e(x = 0)$  is given, we can directly use **Eq. (26)** to solve this boundary flux sweeping problem. For the decoupled Picard iteration approach, we may need to introduce an unknown reference potential to  $\Omega_l$  using either the LCM or DSM method, and then iteratively determine this unknown along the way to obtain a self-consistent system solution pair  $(\phi_e, \phi_l)$ .

## 5 Examples and Analysis

To validate and analyze the numerical methods developed in **Section 3** and **Section 4**, we apply them to some examples based on the model geometry shown in **Figure 1**. The examples consider the charging process at a negative porous electrode, where the following reduction reaction occurs:



This reaction describes the reduction of a trivalent species ( $\text{Ox}^{3+}$ ) to a divalent species ( $\text{Red}^{2+}$ ) via a single electron transfer. **Table 4** summaries the physical and operational parameters used in the examples. **Note:** in **Table 4**,  $\sigma$  is corrected using a constant porosity of 0.78 based on a solid electrode material with a conductivity of 1000 S/m.  $\kappa$  is calculated using the concentrations of  $\text{Ox}^{3+}$  and  $\text{Red}^{2+}$ , set to 1053 mol/m<sup>3</sup> and 27 mol/m<sup>3</sup>, respectively, and is corrected using the same porosity value of 0.78. The relevant formulas and correlations can be found in [15], [16], and [32].

In this section, we focus our discussion on the galvanostatic solution, as the potentiostatic case follows a more standard numerical approach, except in scenarios where the boundary current is swept. Such cases can be regarded as a variant of the galvanostatic solution using the **DSM** approach. Consequently, aside from **Section 5.1**, where we compare numerical solutions with their “exact” counterparts, the subsequent examples and analyses pertain to galvanostatic solutions.

All numerical solutions, except for the global constraining cases, are obtained using BICGSTAB as the linear solver with an ILU preconditioner. In ILU, any zero diagonal entries in the upper triangular factor  $U$  are replaced by a local drop tolerance ( $1 \times 10^{-3}$ ) to prevent singularity. Additionally, all simulations are performed on a Macintosh machine with an M3 Apple Silicon chip and 24 GB of RAM.

### 5.1 Comparison with “Exact” Solutions

We first compare our numerical solutions against their “exact” counterparts. For this purpose, we consider the case with homogeneous electrical and ionic conductivities ( $\sigma$  and  $\kappa$ ), making it possible to derive an analytical expression for the corresponding exact solution in a one-dimensional setting.

**Table 4: Physical and operational parameters used in the examples**

Symbol	Description	Value
<i>Electrode Geometry:</i>		
$W$	Porous electrode width (m)	$5 \times 10^{-3}$
$H$	Porous electrode height (m)	$1 \times 10^{-1}$
$L$	Porous electrode length (m)	$1 \times 10^{-1}$
<i>Physical Parameters:</i>		
$\sigma$	Electrical conductivity of the porous electrode (S/m)	103.1891
$\kappa$	Ionic conductivity of the electrolyte (S/m)	5.9514
$s$	Specific surface area of the porous electrode ( $\text{m}^{-1}$ )	$1.64 \times 10^4$
$\alpha$	Electron transfer coefficient (-)	0.5
$j_0$	Exchange current density ( $\text{A}/\text{m}^2$ )	2.7657
$E_{eq}$	Equilibrium potential (V)	-0.1609
$F$	Faraday constant (C/mol)	96485
$R$	Ideal gas constant ( $\text{J}/(\text{mol} \cdot \text{K})$ )	8.314
$T$	Operating temperature (K)	298.15
<i>Operational Parameters:</i>		
$I_{\text{applied}}$	Applied galvanostatic current (A)	(0, 10]
$V_{\text{applied}}$	Applied potentiostatic electrode potential (V)	0
$V_{\text{sweep}}$	Sweeping potentiostatic electrolyte potential at $x = W$ (V)	[0.1, 0.5]
$I_{\text{sweep}}$	Sweeping potentiostatic current at $x = W$ (A)	(0, 10]

Under this simplification, we rewrite **Eqs. (3a)** and **(3b)** as

$$\frac{d^2 \phi_e}{dx^2} = \frac{a}{\sigma} \sinh(b\eta) \quad (30a)$$

$$\frac{d^2 \phi_l}{dx^2} = -\frac{a}{\kappa} \sinh(b\eta) \quad (30b)$$

where  $a = 2sj_0$  and  $b = \frac{0.5F}{RT}$ . We then subtract **Eq. 30b** from **Eq. 30a**, and apply some basic linear operations ( $\frac{d^2 \phi_e}{dx^2} - \frac{d^2 \phi_l}{dx^2} = \frac{d^2(\phi_e - \phi_l)}{dx^2} = \frac{d^2(\eta + E_{eq})}{dx^2} = \frac{d^2 \eta}{dx^2}$ ), we then obtain:

$$\frac{d^2 \eta}{dx^2} = c \sinh(b\eta) \quad (31)$$

where  $c = (\frac{a}{\sigma} + \frac{a}{\kappa})$ . Using First Integral Method [46], we can derive the following expression for its exact solution (see **Appendix D**):

$$x = \int_{\eta_1}^{\eta} \frac{d\eta}{\sqrt{\frac{2c}{b} \cosh(b\eta) + q_1^2 - \frac{2c}{b} \cosh(b\eta_1)}} \quad (32)$$

where  $\eta_1 = \eta(0)$  and  $q_1 = \frac{d\eta}{dx}|_{x=0}$ . **Eq. (32)** defines an implicit relation between  $x$  and  $\eta(x)$ . It may be more feasible to evaluate this elliptic integral numerically and we also need to know both  $\eta_1$  and

$q_1$ , which are not directly given as discussed in **Section 2**. For the galvanostatic and potentiostatic cases, it is easier to obtain either  $(\eta_1, \eta_2)$  or  $(q_1, q_2)$ , where  $\eta_2 = \eta(W)$  and  $q_2 = \frac{d\eta}{dx}|_{x=W}$ . Thus, we instead apply the shooting method [47], commonly used in solving in boundary-value ODE problems, to find  $\eta_1$  if we know  $(q_1, q_2)$ , or  $q_1$  when we have  $(\eta_1, \eta_2)$ .

For the galvanostatic case, we can readily determine that  $q_1 = \frac{j_{\text{applied}}}{\sigma}$  and  $q_2 = -\frac{j_{\text{applied}}}{\kappa}$  from **Eqs. (4)** and **(5)**. For the potentiostatic case, we need to consider two setups, either sweeping boundary current or boundary potential at  $x = W$ . When the boundary current is being swept there ( $q_2$  is known), we can derive  $q_1 = -\frac{\kappa}{\sigma} q_2$  using charge conservation (**Eq. (13)**). However, for the scenario boundary potential being swept at  $x = W$ , we lack  $(\phi_l(0), \phi_e(W))$  to calculate  $(\eta_1, \eta_2)$ . We may need to use the numerical solver introduced in **Section 4** to obtain those boundary values.

In **Figure 2** and **Figure 3**, we plot the numerical solutions against their respective “exact” solutions, as well as the  $L_2$  and  $H_1$  error reduction as mesh refined. The numerical solutions align very well with their corresponding “exact” solutions and exhibit quadratic error reduction with respect to grid size, demonstrating the accuracy and correctness of the proposed methods.

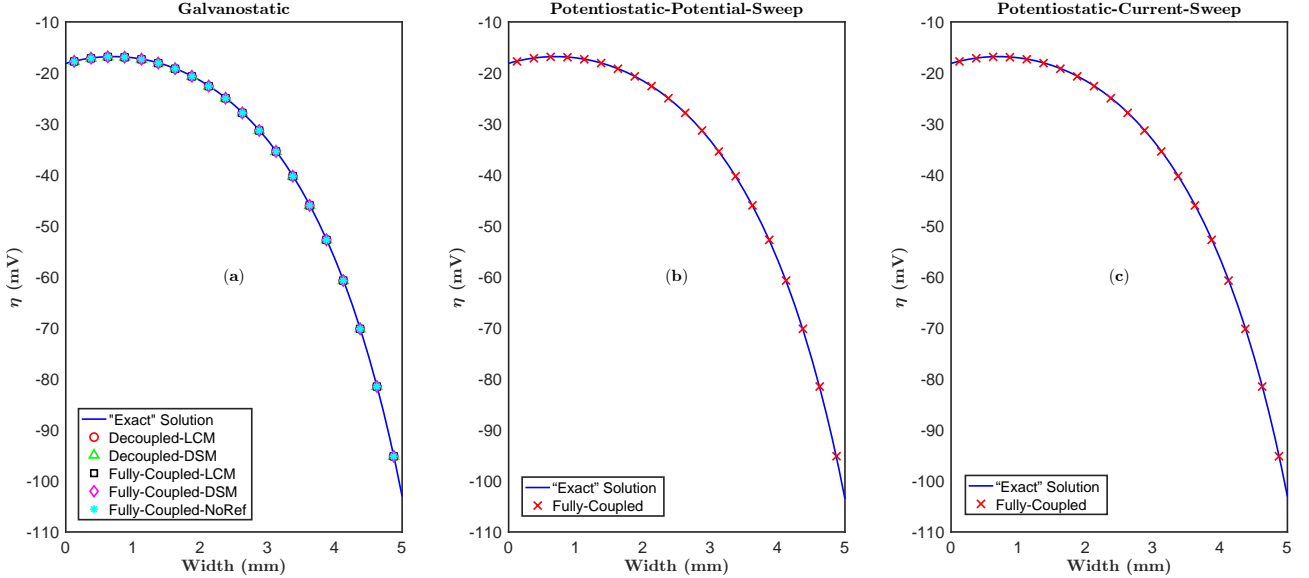


**Figure 2: Numerical vs “exact” solutions. (a): Galvanostatic; (b): Potentiostatic with potential sweep; (c): Potentiostatic with current sweep**

## 5.2 Objective Function for Finding the Electrolyte Reference Potential

As mentioned in **Section 3**, the reference potential for  $\Omega_l$  needs to be self-determined during the solution process if a decoupled scheme is used. This self-determination is carried out as a search problem, guided by the objective function (**Eq. (18)**), which enforces the compatibility between the boundary flux and sink/source term. Since no straightforward analytical expression exists for the objective function, we numerically approximate its discrete realization by sampling the parameter space of the electrolyte reference potential.

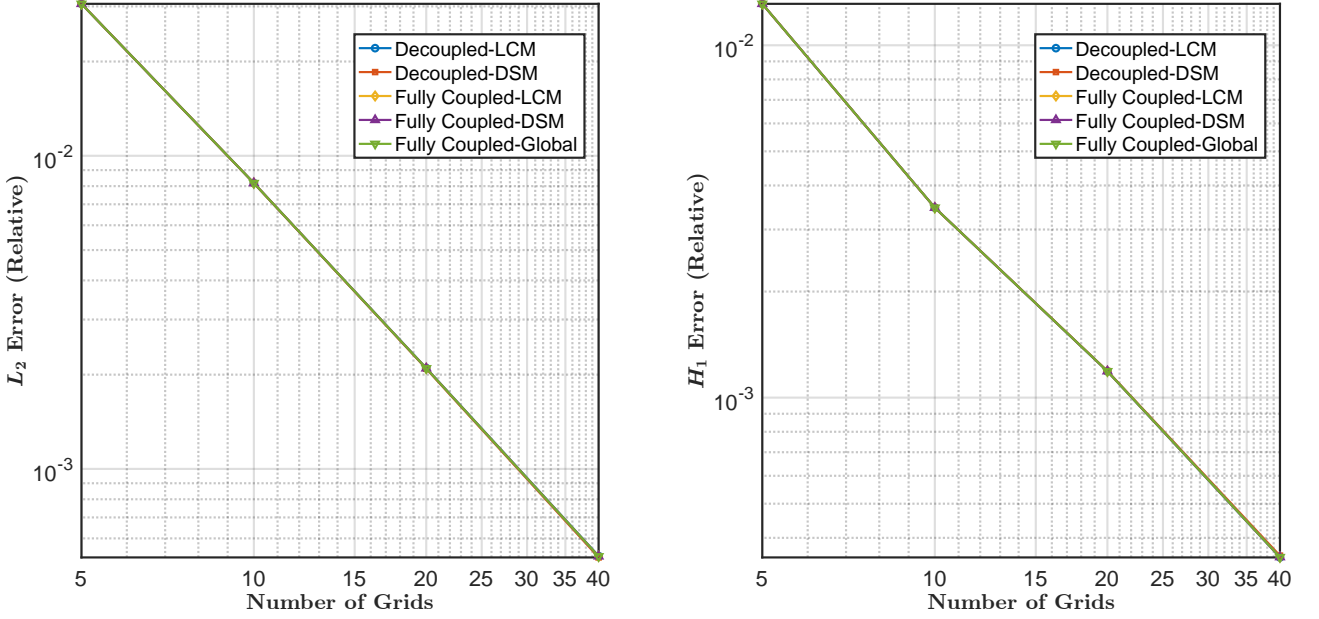


**Figure 3: Error reduction ( $L_2$ ,  $H_1$ )**

**Figure 4** presents the objective function for  $j_{\text{applied}} = 100 \text{ A/m}^2$ . Extensive sampling across various values of  $j_{\text{applied}}$  indicates that the objective function consistently follows a similar piecewise-like trend. It remains flat at lower electrolyte reference potentials to the left of the minimum value. Beyond the minimum point, the function rises sharply, indicating the system’s sensitivity to the chosen reference potential. Deviations to the right of the minimum result in amplified discrepancies. The shape of the function, particularly its “V”-like curve near the minimum, suggests that quadratic optimization methods such as Newton’s method may not be suitable, as the second-order derivative is unlikely to provide helpful information in this region. Gradient descent, which relies on the first-order derivative, may also encounter difficulties near the tip of the curve, as it could lead to oscillations without proper step-size adaptation. A carefully designed step-size adjustment strategy is beneficial to avoid such issues. Alternatively, derivative-free optimization techniques, such as the Golden-section Search [48], may also perform well for this type of objective function.

### 5.3 Homogeneous vs. Heterogeneous

The potential and local current density distributions for homogeneous and heterogeneous conductivity fields are illustrated in **Figure 5**, **Figure 7**, and **Figure 9**. Since the results obtained from different methods are very close, we present only the galvanostatic results obtained using **LCM** with the fully coupled scheme for the case of  $j_{\text{applied}} = 1000 \text{ A/m}^2$ . The computational grid is structured with dimension of 50-by-50.

For the homogeneous case,  $\phi_e$ ,  $\phi_l$ ,  $\eta$ , and  $j$  exhibit smooth gradients.  $\phi_l$  is significantly larger than  $\phi_e$  because  $\sigma$  is about 17 times larger than  $\kappa$ , leading to a greater potential drop in the electrolyte domain.  $\eta$  is lowest near the current collector ( $x = 0$ ) and highest near the separator ( $x = W$ ), confirming reaction dominance near the separator.  $j$  is highly localized near the separator, driven

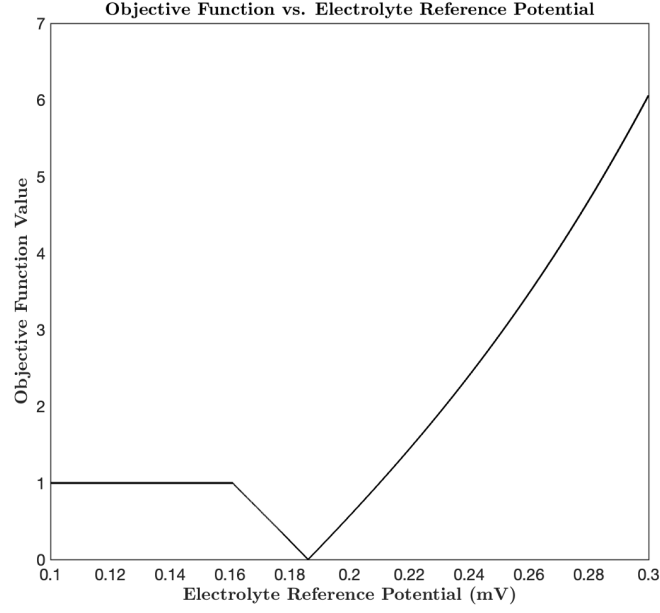


**Figure 4: Objective function**

by the electrolyte's large potential drop. These results align with physical expectations, verifying the accuracy of the numerical solver.

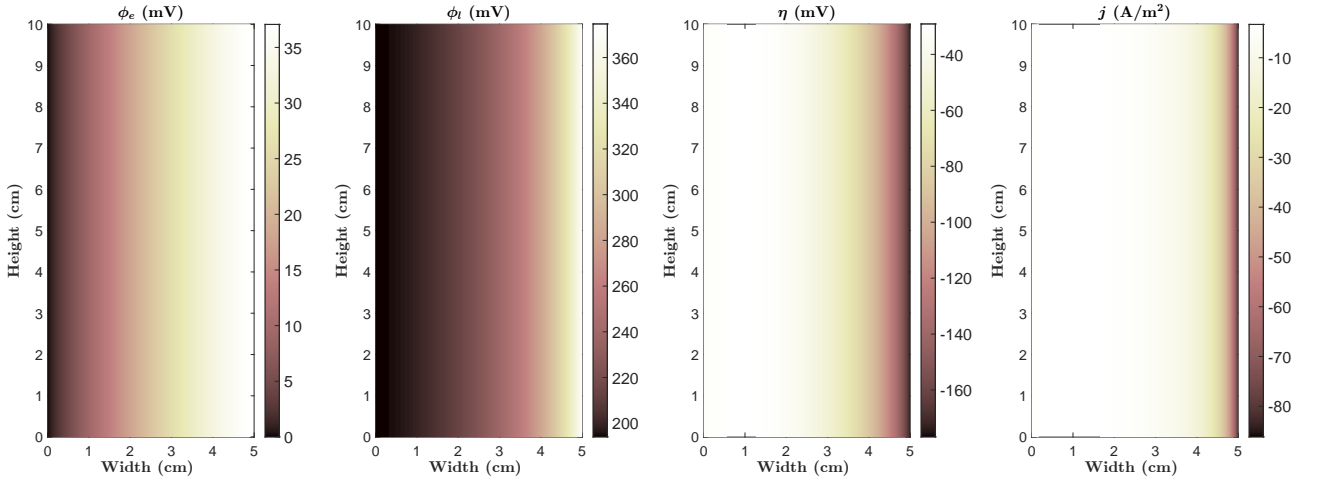


**Figure 5: Potential ( $\phi_e$ ,  $\phi_l$ ,  $\eta$ ) and local current density distributions ( $j$ ) [Galvanostatic,  $j_{\text{applied}} = 1000 \text{ A/m}^2$ , homogeneous  $\sigma$  and  $\kappa$ , x-axis is scaled by 10 times]**

We also generate randomized bimodal conductivity fields for  $\sigma$  and  $\kappa$  to evaluate solver performance under heterogeneous conditions. The heterogeneity originates from spatial variations in the porosity of the porous electrode material. We first initialize a structured 2D porosity field with a low-porosity base value ( $\epsilon_{\text{low}} = 0.2$ ). High-porosity patches ( $\epsilon_{\text{high}} = 0.8$ ) are then introduced using a polygonal tiling scheme. To add connectivity in this 2D model, neighboring high-porosity patches are randomly

linked (if they are not already). Finally, the Bruggeman correction is applied to compute the resulting bimodal conductivity fields for  $\sigma$  and  $\kappa$ . **Figure 6** provides a realization of those two bimodal conductivity fields.

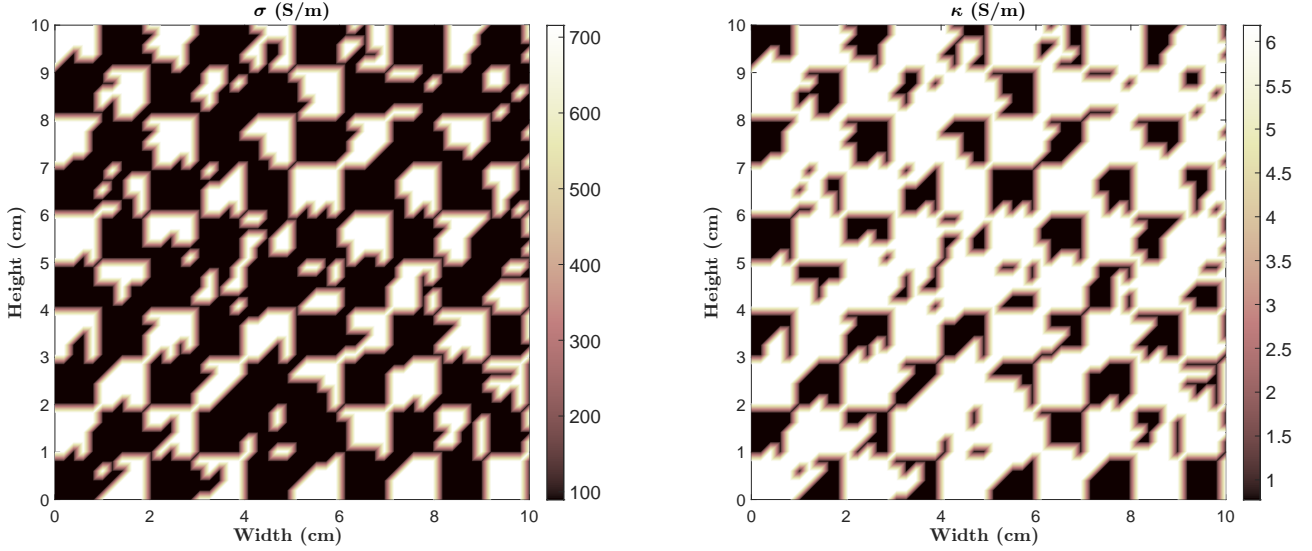


**Figure 6: Bimodal porous electrode conductivity ( $\sigma$ ) field and electrolyte conductivity ( $\kappa$ ) field [x-axis is scaled by 20 times]**

The corresponding overpotential ( $\eta$ ) and local current density ( $j$ ) distributions are shown in **Figure 7**. The heterogeneous conductivity distribution significantly alters the spatial characteristics of the overpotential ( $\eta$ ) and local current density ( $j$ ) fields. Unlike the homogeneous case, the contour patterns exhibit strong irregularities due to the bimodal nature of  $\sigma$  and  $\kappa$ . Reaction localization is evident near the separator (right boundary), where electrolyte-dominated process leads to higher overpotentials. Additionally, the jagged features in  $j$  suggest current crowding effects, highlighting the impact of microstructural connectivity on charge transport efficiency.

We further test a channelized conductivity field (**Figure 8**). To achieve this, we generate a randomly channelized porosity field using a stochastic random-walk approach with lateral perturbations. A set number of channels, determined as a fraction of  $N_y$ , are randomly seeded along the right boundary. Each channel then propagates toward the left with a fixed forward step size while undergoing small random perturbations in the vertical direction, introducing a meandering effect. The lateral displacement is constrained within a predefined perturbation limit to maintain realistic channel connectivity. Additionally, with a given probability  $p_{\text{branch}}$ , a secondary channel may emerge at a nearby location, enhancing the overall connectivity of the network. Once the primary channels reach the right boundary, an additional connectivity refinement step is applied, randomly linking high-porosity regions to ensure a continuous flow path across the domain.

**Figure 9** presents the distributions of overpotential ( $\eta$ ) and local current density ( $j$ ) for the channelized conductivity case. The contour plots reveal the spatial heterogeneity of intensified overpotential and local current density introduced by the channelized conductivity field. These localized variations in  $\eta$  and  $j$  highlight the impact of channel connectivity on electrochemical performance. In together with the bimodal case, these validation examples demonstrate the capability of the introduced numerical

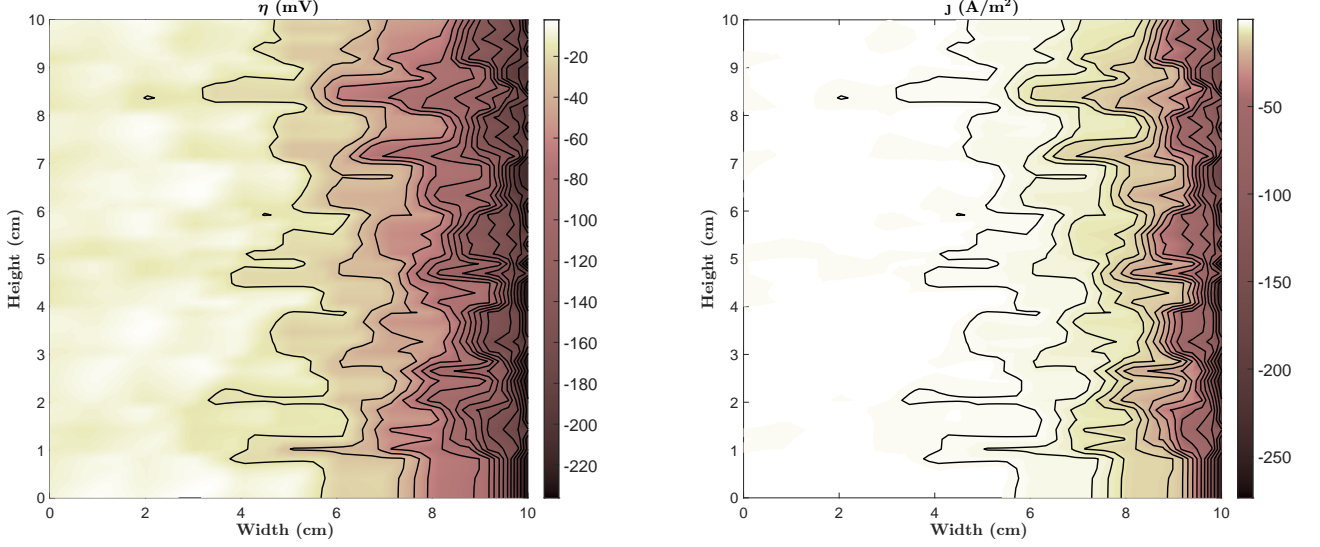


**Figure 7:** Overpotential ( $\eta$ ) field and local current density ( $j$ ) field of the bimodal conductivity case [ $j_{\text{applied}} = 1000 \text{ A/m}^2$ , x-axis is scaled by 20 times]

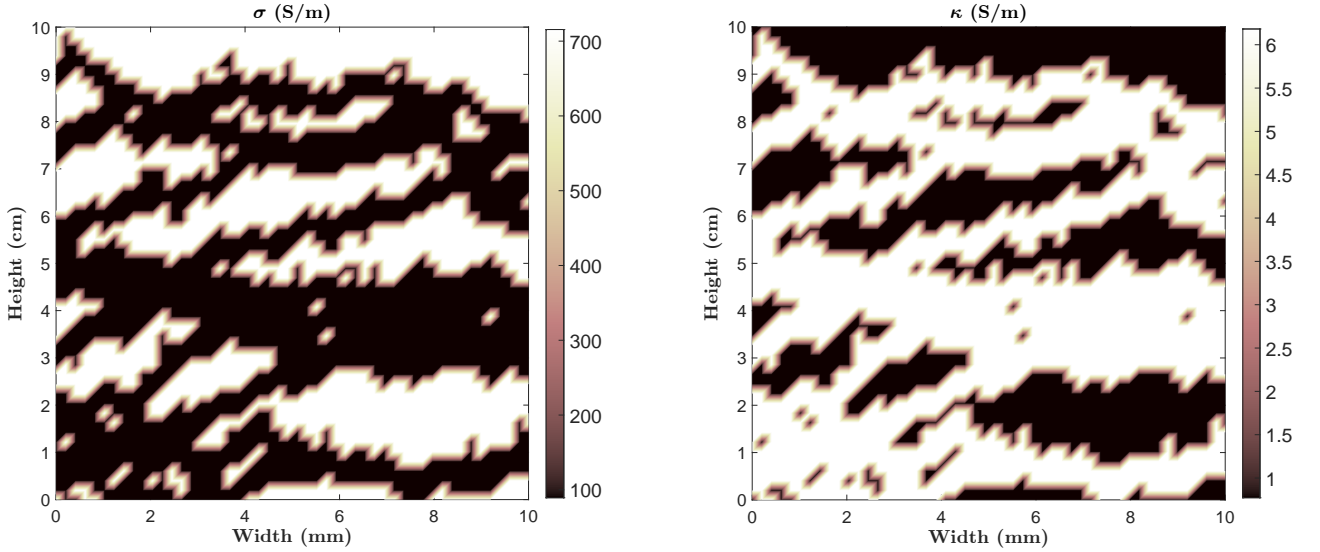


**Figure 8:** Channelized porous electrode conductivity ( $\sigma$ ) field and electrolyte conductivity ( $\kappa$ ) field [x-axis is scaled by 20]

methods in handling heterogeneous conductivity fields.

#### 5.4 Decoupled vs. Fully Coupled

-The decoupled solution scheme introduced in **Section 3.3.1** requires an additional iteration step to determine a reference potential value  $\Omega_l$  that remains self-consistent with the coupled system dynamics. To perform this search, we employ a gradient descent-based line search approach. Since this involves

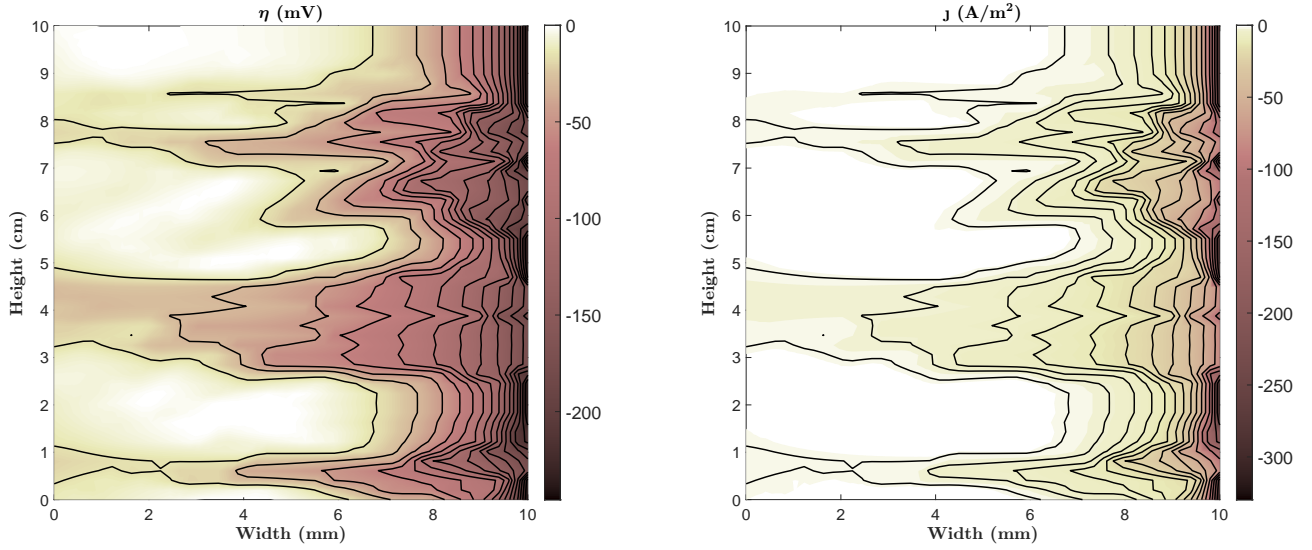


**Figure 9: Overpotential ( $\eta$ ) field and local current density ( $j$ ) field of the channelized conductivity case [ $j_{\text{applied}} = 1000 \text{ A/m}^2$ , x-axis is scaled by 20]**

only a single parameter,  $c_l$ , the search process itself is both robust and scalable with problem size. As shown in **Figure 10**, increasing the number of grid points does not affect the convergence behavior of the  $c_l$  search, demonstrating that it remains approximately independent of  $N$  for both **LCM** and **DSM** (For those case runs, **LCM** generally use about 20 % less iterations than **DSM**). However, this additional search step significantly increases the overall computational complexity. Each update of  $c_l$  requires multiple iterations of line search, where the two Poisson equations are solved two times per iteration [38]. Additionally, each sequential solution of the two equations involves multiple Picard iterations. Although the decoupled scheme involves solving two smaller linear systems—each half the size of the fully coupled scheme—the extra search can easily introduce a computational overhead that is up to hundreds of times greater than that of the fully coupled approach. Consequently, despite its relatively simpler implementation, the decoupled scheme is not a practical choice due to the excessive computational cost.

In contrast, the fully coupled scheme solves the two Poisson equations only once. As shown in **Figure 11**, the fully coupled scheme, when equipped using **LCM** and **DSM**, demonstrates excellent scalability, even for the highly heterogeneous cases. From those case runs, **DSM** outperforms **LCM** for the homogeneous case and roughly performs the same as **LCM** for the heterogeneous case.

**Note:** We use the bimodal heterogeneity case because it presents greater numerical challenges in solving the underlying PDEs compared to the channelized cases. The primary difficulties arise from the blocky heterogeneity and discontinuities, leading to large numerical gradient and potential errors. The high contrast regions can increase the condition number of the discretized system, slowing convergence. Additionally, numerical diffusion effects may smooth out sharp interfaces, reducing accuracy.

**Remark 5.1.** For the decoupled solution, running a full Picard iteration is not necessary, as the search algorithm only requires an estimate of the search gradient. Therefore, we perform only one Picard iteration per  $(\phi_e, \phi_l)$  solve, and the final solution remains identical to cases using full Picard iterations. Additionally, alternative search algorithms, such as the Golden Section Search, may require



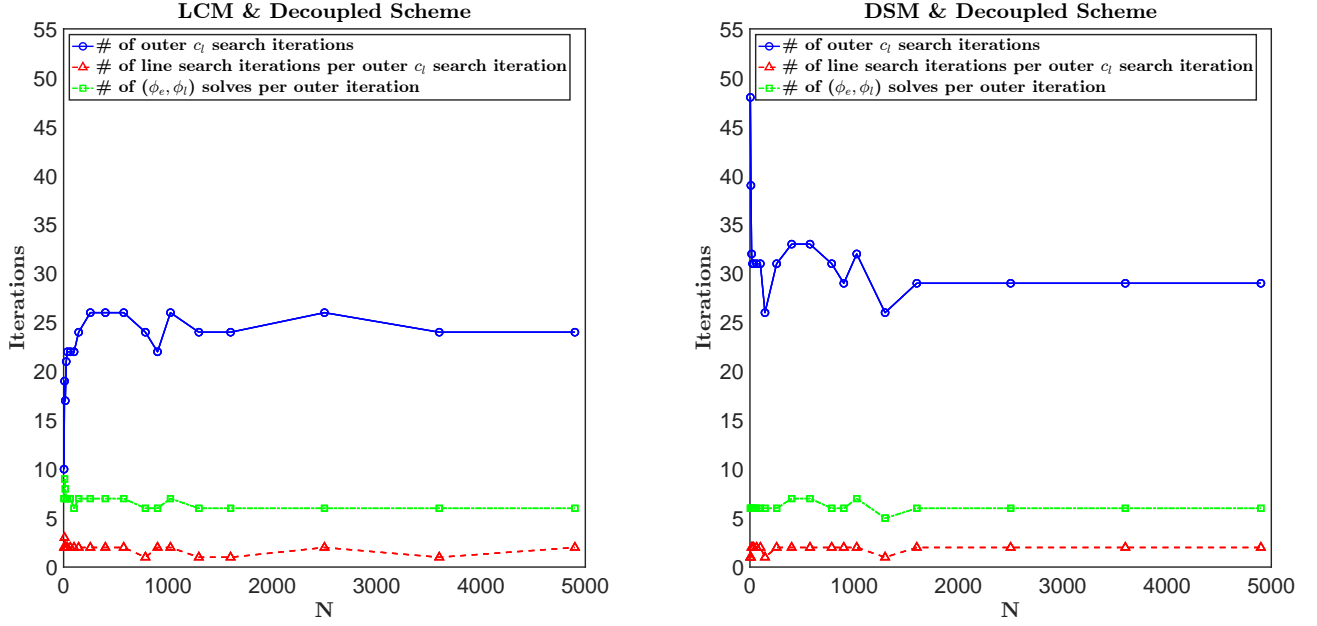


Figure 10: Iteration performance of the decoupled Scheme using LCM and DSM ( $j_{\text{applied}} = 500 \text{ A/m}^2$ ,  $N$  is the size of Jacobian Matrix. The global residual tolerance is  $1 \times 10^{-6}$ )

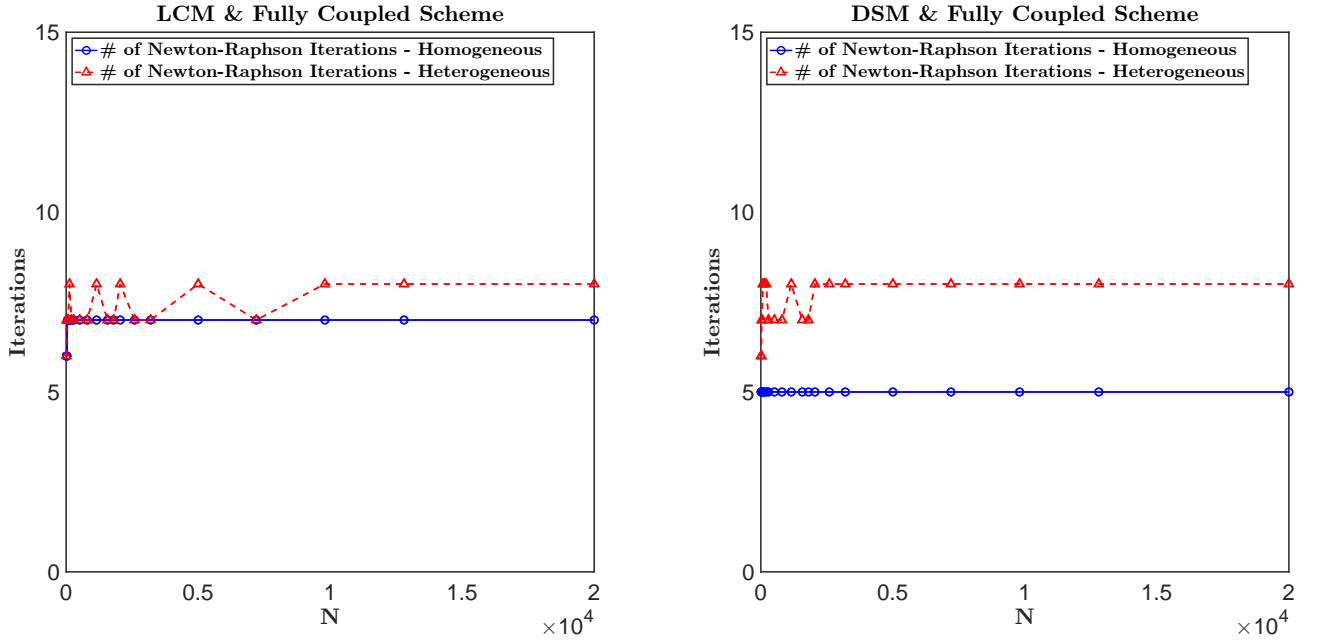


Figure 11: Iteration performance of the fully coupled scheme using LCM and DSM ( $j_{\text{applied}} = 500 \text{ A/m}^2$ ,  $N$  is the size of Jacobian Matrix. The global residual tolerance is  $1 \times 10^{-6}$ . The heterogeneity is the bimodal case)

fewer intermediate  $(\phi_e, \phi_l)$  solves. Nevertheless, as long as searching for  $c_l$  is required, the fully coupled

scheme remains a much more attractive choice.

**Remark 5.2.** *Newton-Raphson is used for linearization, and the solution of this problem is sensitive to the initialization of  $(\phi_e, \phi_l)$ . This sensitivity arises because the initial values of  $\phi_e$  and  $\phi_l$  directly affect the computation of the residual vector and the derivative terms in the Jacobian matrix. These computations involve highly nonlinear exponential terms, which can produce extremely large values in both positive and negative directions, often leading to divergence. To ensure stability, we recommend initializing both  $\phi_e$  and  $\phi_l$  to zero. Alternatively,  $\phi_l$  can be initialized to  $-E_{eq}$  while  $\phi_e$  is set to zero. These two options help mitigate numerical instabilities and provide a well-conditioned starting point for the Newton-Raphson iteration.*

**Remark 5.3.** *The convergence performances of **LCM** and **DSM** are found to be similar for the test cases, suggesting that **DSM** may be preferable to **LCM**. This is because, although **LCM** requires only one additional internal constant potential constraint (which means  $\text{size}(J^L) \approx \text{size}(J)$ ), it can still lead to a poorly scaled  $J^L$ , necessitating special rescaling to reduce its condition number, which generally increases the number of linear solver iterations.*

## 5.5 LCM/DSM vs. GCM

To evaluate the performance of the fully coupled scheme using **GCM** (without applying a constant reference potential to the system), we plot the Newton-Raphson convergence for cases using MINRES and LSTR in **Figure 12**. **Note:** We do not compare the performance of the Moore–Penrose pseudoinverse, as this  $\mathcal{O}(N^3)$  approach can rapidly exhausts computational resources. For the homogeneous case, the performance of these methods is identical and closely comparable to the **LCM/DSM** referencing approaches shown in **Figure 11**.

For the heterogeneous case, MINRES struggles to converge to the prescribed tolerance of  $1.0 \times 10^{-6}$ , although Newton-Raphson itself still converges. In contrast, LSTR performs well in the heterogeneous case. It should be noted that due to the singularity, the computational complexities of both MINRES and LSTR are actually comparable at the level of  $\mathcal{O}(N^2)$ . Thus, as shown in **Figure 12**, LSTR is clearly preferable to MINRES, as MINRES requires more iterations.

Inexact linear solver solutions may not hinder the global Newton-Raphson convergence, provided they achieve a residual of  $10^{-2} \sim 10^{-3}$  or better. This suggests that in practical implementations, iterative solvers with moderate accuracy may be preferable to direct solvers, particularly for large-scale problems where computational efficiency is a concern. However, using inexact linear solver solutions can degrade Newton-Raphson convergence from quadratic to linear and may introduce minor oscillations.

To improve the convergence performance of MINRES, we can apply some preconditioning techniques. The Jacobian matrix  $J$  is singular ( $\text{rank} = N - 1$ ) with a null space. To modify the spectral properties of  $J$ , we construct the following augmented system ( $J_{\text{aug}}$ ):

$$J_{\text{aug}} = \begin{bmatrix} J & \lambda I \\ \lambda I & I \end{bmatrix} \quad (33)$$

Here,  $\lambda$  is a regularization parameter, typically ranging from  $10^{-6}$  to  $10^{-2}$ . **Eq. (33)** shifts the singular values away from zero, thereby reducing the condition number. However,  $J_{\text{aug}}$  is twice the size of  $J$ , which introduces an additional computational cost of  $\mathcal{O}(3N)$ . To mitigate this overhead, we can use

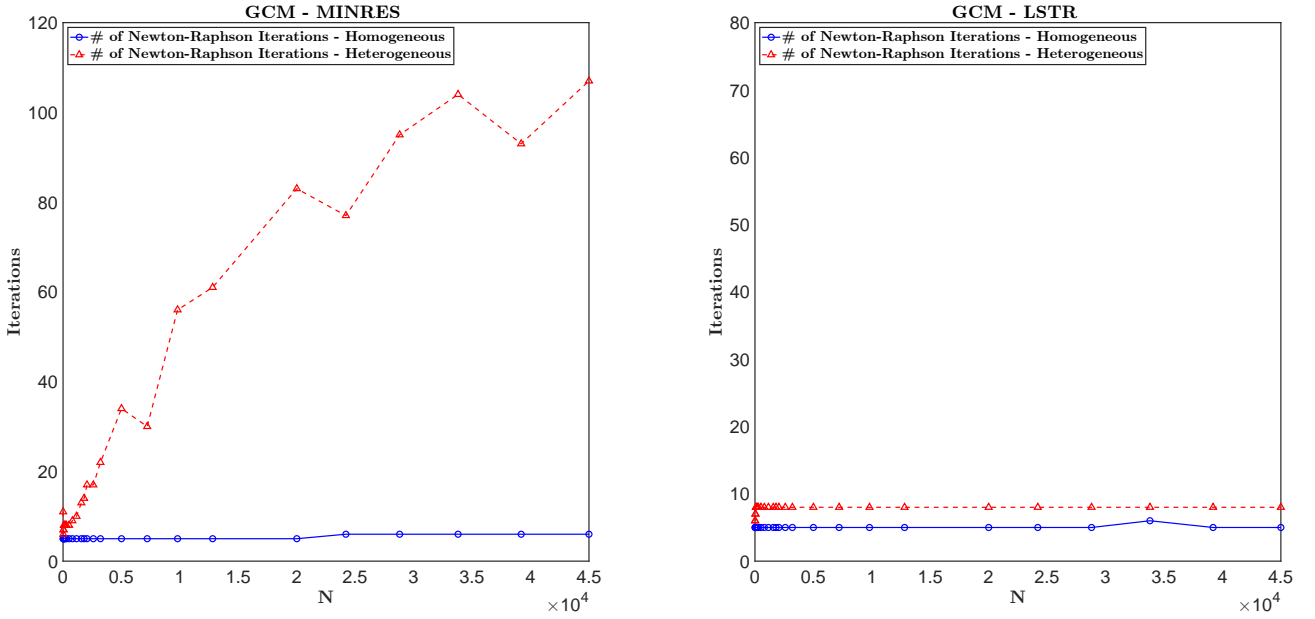


**Figure 12:** Iteration performance of the fully coupled scheme using MINRES and LSTR ( $j_{\text{applied}} = 500 \text{ A/m}^2$ .  $N$  represents the size of the Jacobian matrix. The global residual tolerance is  $1 \times 10^{-6}$ . The heterogeneity is the bimodal case)

the Schur complement to reduce  $J_{\text{aug}}$  to  $J - \lambda^2 I$ . **Figure 13** shows the effect of preconditioning, which reduces the number of iterations. However, it remains higher than LSTR and exhibits an increasing trend as  $N$  grows.

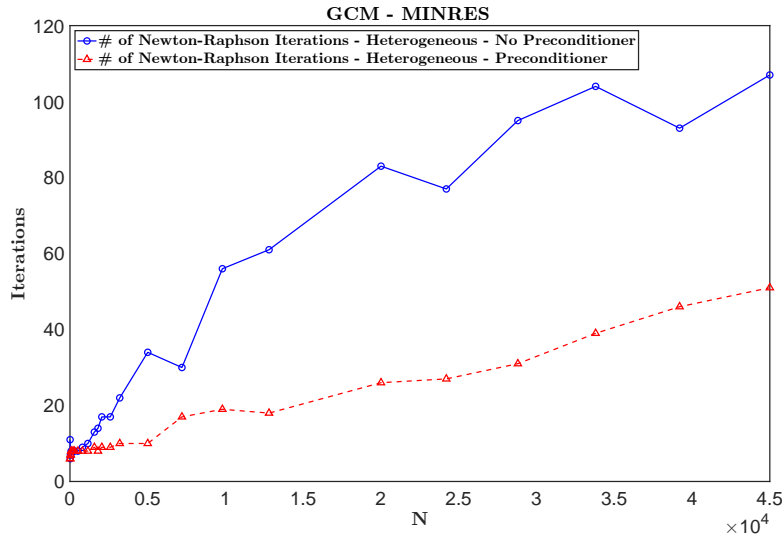


**Figure 13:** Iteration performance of the fully coupled scheme using MINRES with preconditioning ( $j_{\text{applied}} = 500 \text{ A/m}^2$ .  $N$  represents the size of the Jacobian matrix. The global residual tolerance is  $1 \times 10^{-6}$ . The heterogeneity is the bimodal case)

**Remark 5.4.** *If we are only interested in applications with homogeneous conductivity fields, **GCM***

using either *MINRES* or *LSTR* may be a good option, as it eliminates the need to set explicit reference potentials in the system during the solution phase. The values of  $(\phi_e, \phi_l)$  can be recovered as needed through a simple postprocessing step (**Eq. (28)**). For heterogeneous cases, depending on the level of heterogeneity, the computational cost of **GCM** can be significantly higher than that of **LCM/DSM** when using *MINRES*, whereas *LSTR* may incur only a slightly higher cost than **LCM/DSM**, which solve a well-posed system. However, the key takeaway is that for solving  $\phi_e - \phi_l$  or  $\eta$  in galvanostatic problems, this approach enables a solution without requiring any explicit potential references.

## 6 Summary and Conclusions

This work systematically details numerical methods for solving the nonlinearly coupled Poisson equations arising in dual-continuum modeled porous electrode systems. First, we mathematically demonstrate that under galvanostatic conditions, the system admits a unique solution in terms of the potential difference  $\phi_e - \phi_l$  (or  $\eta$ ), with an additional degree of freedom allowing a shared constant shift in the solution spaces of  $\phi_e$  and  $\phi_l$ . This additional degree of freedom leads to an underconstrained and singular system. We then introduce three strategies to address this challenge: **LCM**, **DSM**, and **GCM**. **LCM** is theoretically grounded in Dirichlet’s principle and the Lagrange multiplier method, where a unified energy functional is formulated for the coupled Poisson dynamics. **DSM** is derived from Gauss’s theorem. Both **LCM** and **DSM** require an explicit reference potential, whereas **GCM** allows solving for  $\phi_e - \phi_l$  (or  $\eta$ ) without imposing a reference, providing some levels of flexibility.

Two nonlinear solution schemes, decoupled and fully coupled, are presented and compared. The fully coupled approach exhibits superior performance in terms of efficiency, convergence, and robustness, as the decoupled scheme requires an extra search for finding an additional reference potential to match the system dynamics. In the homogeneous case, **LCM**, **DSM**, and **GCM** yield comparable results. For heterogeneous cases, **GCM** show numerical struggleness when *MINRES* is used as the linear solver, even with preconditioning, whereas *LSTR* solver makes **GCM** remain stable and efficient. The numerical results validate these methods across various conductivity and operating conditions, demonstrating their effectiveness in handling underconstrained singularities, nonlinear source/sink term coupling, and heterogeneities. These methods provide a general framework for addressing similar underconstrained nonlinear systems. A Python implementation of the introduced nonlinear solvers is provided at [https://github.com/harrywang1129/porous\\_electrode\\_solver](https://github.com/harrywang1129/porous_electrode_solver). The code is currently limited to two-dimensional problems with limited flexibility. It should also be noted that this open-source version utilizes linear algebra packages available in *scipy* (such as *splu* and *lsmr*), which may lead to differences in performance relative to the results presented in **Section 5**, where proprietary approaches were used (available upon request) in solving the final linear systems ( $Ax = b$ ). As part of ongoing work, we are extending to a 3D general-purpose multicontinuum advection-diffusion-reaction model, where species transport and electrochemical kinetics are fully coupled for porous electrode devices. The simulator will be open-sourced upon completion.

## Appendix A Solution Uniqueness of Galvanostatic Solution

We prove that the following system admits a unique set of solution pairs  $(\phi_e, \phi_l)$  up to an additive constant:

$$\nabla \cdot (-\sigma \nabla \phi_e) = -f(\eta) \quad \text{in } \Omega_e, \quad (\text{A.1a})$$

$$\nabla \cdot (-\kappa \nabla \phi_l) = f(\eta) \quad \text{in } \Omega_l, \quad (\text{A.1b})$$

$$\sigma \frac{\partial \phi_e}{\partial n} = g_e \quad \text{on } \partial\Omega_e, \quad (\text{A.1c})$$

$$\kappa \frac{\partial \phi_l}{\partial n} = g_l \quad \text{on } \partial\Omega_l. \quad (\text{A.1d})$$

where  $f = a \sinh(b\eta)$  and  $\eta = \phi_e - \phi_l - E_{eq}$ .

Let  $(\phi_e^1, \phi_l^1)$  and  $(\phi_e^2, \phi_l^2)$  be two pairs of solutions to **Eqs. (A.1a)–(A.1d)**. We subtract **Eq. (A.1a)** and **Eq. (A.1b)** for  $\phi_{e/l}^2$  from those equations for  $\phi_{e/l}^1$  and define  $\xi_e := \phi_e^1 - \phi_e^2$ ,  $\xi_l := \phi_l^1 - \phi_l^2$ ,  $\eta^1 := \phi_e^1 - \phi_l^1 - E_{eq}$ , and  $\eta^2 := \phi_e^2 - \phi_l^2 - E_{eq}$ . They satisfy the following equations:

$$\nabla \cdot (-\sigma \nabla \xi_e) = -f(\eta^1) + f(\eta^2),$$

$$\nabla \cdot (-\kappa \nabla \xi_l) = f(\eta^1) - f(\eta^2).$$

Here, the subscripts  $(e/l)$  refer to the electrode and electrolyte, respectively, while the superscripts  $(1/2)$  denote the first and second pairs of solutions.

We then multiply both equations by  $(\xi_e, \xi_l)$  respectively and perform integration over  $\Omega_{e/l}$ , we have:

$$\int_{\Omega_e} \xi_e \nabla \cdot (-\sigma \nabla \xi_e) dx = - \int_{\Omega_e} \xi_e [f(\eta^1) - f(\eta^2)] dx, \quad (\text{A.2a})$$

$$\int_{\Omega_l} \xi_l \nabla \cdot (-\kappa \nabla \xi_l) dx = \int_{\Omega_l} \xi_l [f(\eta^1) - f(\eta^2)] dx. \quad (\text{A.2b})$$

We process the integral terms on the left-hand side by integration by parts and we can arrive at:

$$\int_{\Omega_e} \xi_e \nabla \cdot (-\sigma \nabla \xi_e) dx = \int_{\Omega_e} \sigma |\nabla \xi_e|^2 dx - \int_{\partial\Omega_e} \xi_e \sigma \frac{\partial \xi_e}{\partial n} dS_e,$$

$$\int_{\Omega_l} \xi_l \nabla \cdot (-\kappa \nabla \xi_l) dx = \int_{\Omega_l} \kappa |\nabla \xi_l|^2 dx - \int_{\partial\Omega_l} \xi_l \kappa \frac{\partial \xi_l}{\partial n} dS_l,$$

Since  $\xi_e := \phi_e^1 - \phi_e^2$ ,  $\xi_l := \phi_l^1 - \phi_l^2$ , we know  $\sigma \frac{\partial \xi_e}{\partial n} = 0$  on  $\partial\Omega_e$  and  $\kappa \frac{\partial \xi_l}{\partial n} = 0$  on  $\partial\Omega_l$ . And thus,

$$\int_{\Omega_e} \sigma |\nabla \xi_e|^2 dx = - \int_{\Omega_e} \xi_e [f(\eta^1) - f(\eta^2)] dx, \quad (\text{A.4a})$$

$$\int_{\Omega_l} \kappa |\nabla \xi_l|^2 dx = \int_{\Omega_l} \xi_l [f(\eta^1) - f(\eta^2)] dx. \quad (\text{A.4b})$$

By summing **Eqs. (A.4a)** and **(A.4b)** together, we obtain:

$$\begin{aligned} 0 &\leq \int_{\Omega_e} \sigma |\nabla \xi_e|^2 + \int_{\Omega_l} \kappa |\nabla \xi_l|^2 = - \int_{\Omega} [f(\eta^1) - f(\eta^2)](\xi_e - \xi_l) \, dx \\ &= - \int_{\Omega} [f(\eta^1) - f(\eta^2)](\eta^1 - \eta^2) \, dx. \end{aligned} \quad (\text{A.5})$$

Noticing that

$$f'(\eta) = ab \cosh(b\eta) > 0,$$

we conclude that  $f(\eta)$  is a strictly monotonically increasing function of  $\eta$ . This implies that for any given  $x$ ,

$$\text{if } \eta^1(x) > \eta^2(x) \implies f(\eta^1(x)) > f(\eta^2(x)),$$

$$\text{if } \eta^1(x) < \eta^2(x) \implies f(\eta^1(x)) < f(\eta^2(x)),$$

$$\Downarrow$$

$$\left[ f(\eta^1(x)) - f(\eta^2(x)) \right] (\eta^1(x) - \eta^2(x)) \geq 0, \quad \forall x \in \Omega.$$

Integrating over the entire domain, we obtain

$$- \int_{\Omega} [f(\eta^1) - f(\eta^2)](\eta^1 - \eta^2) \, dx \leq 0.$$

Since the integral is non-negative, the only possibility for equality to hold is when the integrand itself is zero almost everywhere in  $\Omega$ , leading to

$$f(\eta^1) - f(\eta^2) = 0 \quad \text{a.e. in } \Omega. \quad (\text{A.6})$$

Since  $f(\eta)$  is strictly monotonic, this directly implies that

$$\eta^1(x) = \eta^2(x) \quad \text{a.e. in } \Omega.$$

Recalling that  $\eta = \phi_e - \phi_l - E_{\text{eq}}$ , we immediately obtain

$$\xi_e(x) = \xi_l(x) \quad \text{a.e. in } \Omega.$$

Now, looking back at **Eq. (A.5)**, we notice

$$\int_{\Omega} \sigma |\nabla \xi_e|^2 \, dx + \int_{\Omega} \kappa |\nabla \xi_l|^2 \, dx = 0,$$

we conclude that

$$\nabla \xi_e = 0, \quad \nabla \xi_l = 0 \quad \text{a.e. in } \Omega.$$

This implies that both  $\xi_e$  and  $\xi_l$  must be spatially constant in  $\Omega$ , i.e.,

$$\xi_e(x) = \xi_l(x) = C, \quad \text{a.e. in } \Omega$$

for some constant  $C \in \mathbb{R}$ .

Thus, any solution pair  $(\phi_e, \phi_l)$  to the system must be of the form:

$$\{(\phi_e, \phi_l) \mid \phi_e = \phi_e^* + C, \quad \phi_l = \phi_l^* + C, \quad C \in \mathbb{R}\}.$$

where the asterisk (\*) denotes a **particular pair of solutions**. That is,  $\phi_e^*$  and  $\phi_l^*$  represent a specific set of solutions to the system, and any other solutions can be obtained by adding a constant  $C$ .

This completes the proof that the solution pair to the coupled nonlinear Neumann Poisson system is **unique up to an additive constant  $C$** .

## Appendix B Dirichlet's Principle and Lagrange Multiplier

We consider here a coupled Poisson system under all-Neumann boundary conditions in the following general form:

$$\nabla \cdot (-\sigma \nabla \phi_1) = -f(\phi_1 - \phi_2) \quad \text{in } \Omega, \quad (\text{B.1a})$$

$$\nabla \cdot (-\kappa \nabla \phi_2) = f(\phi_1 - \phi_2) \quad \text{in } \Omega, \quad (\text{B.1b})$$

$$\sigma \frac{\partial \phi_1}{\partial n} = g_1 \quad \text{on } \partial\Omega, \quad (\text{B.1c})$$

$$\kappa \frac{\partial \phi_2}{\partial n} = g_2 \quad \text{on } \partial\Omega. \quad (\text{B.1d})$$

where  $f(\phi_1 - \phi_2) = a \sinh[b(\phi_1 - \phi_2 - E_{eq})]$ , and  $a$  and  $b$  are some constants.

Based on Dirichlet's principle, We try to write a unified energy functional for this system as

$$\mathcal{E}(\phi_1, \phi_2) = \frac{1}{2} \int_{\Omega} \sigma |\nabla \phi_1|^2 + \frac{1}{2} \int_{\Omega} \kappa |\nabla \phi_2|^2 - \int_{\Omega} V(\phi_1, \phi_2) - \int_{\partial\Omega} g_1 \phi_1 - \int_{\partial\Omega} g_2 \phi_2 \quad (\text{B.2})$$

where:

- $\frac{1}{2} \int_{\Omega} \sigma |\nabla \phi_1|^2$  and  $\frac{1}{2} \int_{\Omega} \kappa |\nabla \phi_2|^2$  represents the respective energy associated with the gradients of  $\phi_1$  and  $\phi_2$ , penalizing variations in  $\phi_1$  and  $\phi_2$  within  $\Omega$ ;
- $V(\phi_1, \phi_2)$  is a potential energy term accounting for the interaction between the source/sink term  $(-f, f)$  and  $(\phi_1, \phi_2)$  within  $\Omega$ ;
- $\int_{\partial\Omega} g_1 \phi_1$  and  $\int_{\partial\Omega} g_2 \phi_2$  incorporates the contributions of the Neumann boundary fluxes  $g_1$  and  $g_2$  to the energy of the coupled system.

For  $V(\phi_1, \phi_2)$ , we have that its partial derivative with respect to  $\phi_1$  yields  $-f(\phi_1 - \phi_2)$  and with respect to  $\phi_2$  yields  $f(\phi_1 - \phi_2)$ . In a matrix form, we can express as:

$$\begin{bmatrix} \frac{\partial V(\phi_1, \phi_2)}{\partial \phi_1} \\ \frac{\partial V(\phi_1, \phi_2)}{\partial \phi_2} \end{bmatrix} = \begin{bmatrix} -f(\phi_1 - \phi_2) \\ f(\phi_1 - \phi_2) \end{bmatrix}. \quad (\text{B.3})$$

**Note:** For the case of **Eqs. (3a)–(3b)**, a natural choice for such potential function is

$$V(\phi_e, \phi_l) = -\frac{a}{b} \cosh(b\eta) \quad (\text{B.4})$$

with  $\eta = \phi_e - \phi_l - E_{eq}$ .

Next, we perform variational analysis to **Eq. (B.2)** by introducing a small perturbation to  $\phi_1$  such that:

$$\phi_1^{\epsilon_1} = \phi_1 + \epsilon_1 v_1, \quad (\text{B.5})$$

where  $\epsilon_1$  is an arbitrary small variable, and  $v_1$  is an arbitrary smooth function.

Plug **Eq. (B.5)** in, we have:

$$\begin{aligned} \mathcal{E}(\phi_1^{\epsilon_1}, \phi_2) &= \frac{1}{2} \int_{\Omega} \sigma |\nabla(\phi_1 + \epsilon_1 v_1)|^2 + \frac{1}{2} \int_{\Omega} \kappa |\nabla \phi_2|^2 - \int_{\Omega} V[(\phi_1 + \epsilon_1 v_1), \phi_2] \\ &\quad - \int_{\partial\Omega} g_1(\phi_1 + \epsilon_1 v_1) - \int_{\partial\Omega} g_2 \phi_2 \end{aligned} \quad (\text{B.6})$$

Here  $|\nabla(\phi_1 + \epsilon_1 v_1)|^2 = |\nabla \phi_1|^2 + 2\epsilon_1 \nabla \phi_1 \cdot \nabla v_1 + \epsilon_1^2 |\nabla v_1|^2$ .

Differentiate **Eq. (B.6)** with respect to  $\epsilon_1$  and evaluate at  $\epsilon_1 = 0$ , then:

$$\left. \frac{\partial}{\partial \epsilon_1} \left( \frac{1}{2} \int_{\Omega} \sigma |\nabla(\phi_1 + \epsilon_1 v_1)|^2 \right) \right|_{\epsilon_1=0} = \int_{\Omega} \sigma \nabla \phi_1 \cdot \nabla v_1 \quad (\text{B.7a})$$

$$= \int_{\Omega} \nabla \cdot (-\sigma \nabla \phi_1) v_1 + \int_{\partial\Omega} \sigma \frac{\partial \phi_1}{\partial n} v_1, \quad (\text{B.7b})$$

$$\left. \frac{\partial}{\partial \epsilon_1} \left( \int_{\Omega} V[(\phi_1 + \epsilon_1 v_1), \phi_2] \right) \right|_{\epsilon_1=0} = \int_{\Omega} -f(\phi_1 - \phi_2) v_1, \quad (\text{B.7c})$$

$$\left. \frac{\partial}{\partial \epsilon_1} \left( \int_{\partial\Omega} g_1(\phi_1 + \epsilon_1 v_1) \right) \right|_{\epsilon_1=0} = \int_{\partial\Omega} g_1 v_1. \quad (\text{B.7d})$$

Similarly, if we perform the variation with respect to  $\phi_2$ , we have:

$$\left. \frac{\partial}{\partial \epsilon_2} \left( \frac{1}{2} \int_{\Omega} \kappa |\nabla(\phi_2 + \epsilon_2 v_2)|^2 \right) \right|_{\epsilon_2=0} = \int_{\Omega} \kappa \nabla \phi_2 \cdot \nabla v_2 \quad (\text{B.8a})$$

$$= \int_{\Omega} \nabla \cdot (-\kappa \nabla \phi_2) v_2 + \int_{\partial\Omega} \kappa \frac{\partial \phi_2}{\partial n} v_2, \quad (\text{B.8b})$$

$$\left. \frac{\partial}{\partial \epsilon_2} \left( \int_{\Omega} V[\phi_1, (\phi_2 + \epsilon_2 v_2)] \right) \right|_{\epsilon_2=0} = \int_{\Omega} f(\phi_1 - \phi_2) v_2, \quad (\text{B.8c})$$

$$\left. \frac{\partial}{\partial \epsilon_2} \left( \int_{\partial\Omega} g_2(\phi_2 + \epsilon_2 v_2) \right) \right|_{\epsilon_2=0} = \int_{\partial\Omega} g_2 v_2. \quad (\text{B.8d})$$

Thus, we have:

$$\left. \frac{\partial \mathcal{E}(\phi_1^{\epsilon_1}, \phi_2^{\epsilon_2})}{\partial(\epsilon_1, \epsilon_2)} \right|_{\epsilon_1=0, \epsilon_2=0} = \left[ \int_{\Omega} \nabla \cdot (-\sigma \nabla \phi_1) v_1 + \int_{\Omega} f(\phi_1 - \phi_2) v_1 - \int_{\partial\Omega} (g_1 - \sigma \frac{\partial \phi_1}{\partial n}) v_1 \right. \\ \left. - \int_{\Omega} \nabla \cdot (-\kappa \nabla \phi_2) v_2 - \int_{\Omega} f(\phi_1 - \phi_2) v_2 - \int_{\partial\Omega} (g_2 - \kappa \frac{\partial \phi_2}{\partial n}) v_2 \right] \quad (\text{B.9})$$



To minimize the energy functional  $\mathcal{E}(\phi_1, \phi_2)$ , we set **Eq. (B.9)** to zero such that:

$$\left. \frac{\partial \mathcal{E}(\phi_1^{\epsilon_1}, \phi_2^{\epsilon_2})}{\partial(\epsilon_1, \epsilon_2)} \right|_{\epsilon_1=0, \epsilon_2=0} = \begin{bmatrix} 0 \\ 0 \end{bmatrix} \quad (\text{B.10})$$

Since  $v_1$  and  $v_2$  are arbitrary, **Eq. (B.10)** hold if and only if:

$$\nabla \cdot (-\sigma \nabla \phi_1) = -f(\phi_1 - \phi_2) \quad \text{in } \Omega, \quad (\text{B.11a})$$

$$\nabla \cdot (-\kappa \nabla \phi_2) = f(\phi_1 - \phi_2) \quad \text{in } \Omega, \quad (\text{B.11b})$$

$$\sigma \frac{\partial \phi_1}{\partial n} = g_1 \quad \text{on } \partial\Omega, \quad (\text{B.11c})$$

$$\kappa \frac{\partial \phi_2}{\partial n} = g_2 \quad \text{on } \partial\Omega. \quad (\text{B.11d})$$

We can see that the above obtained Euler–Lagrange equations exactly recover **Eqs. (B.1a)–(B.1b)**, and honor the original Neumann boundary conditions as in **Eqs. (B.1c)–(B.1d)**. By constructing a unified energy functional in this manner, even when the coefficients  $\sigma$  and  $\kappa$  differ, the variational formulation recovers the original coupled system in its entirety.

**Remark Appendix B.1.** *If the nonlinear term lacks antisymmetry, then no potential function  $V(\phi_1, \phi_2)$  can reproduce **Eq. (B.3)**, provided the reaction current density depends on  $\phi_1 - \phi_2$ . In other words, the system cannot be derived from a single unified energy functional when the coefficients of the nonlinear terms in the two equations are not balanced. This violates the principle of “conservativity” or “self-adjointness.” Consequently, if such coupled system is governed by an asymmetric nonlinear source/sink term, it is inherently impossible to construct a single energy functional to describe it.*

Now, based on the unified energy functional (**Eq. (B.2)**), let us add some local Lagrange constraints to the coupled system. Suppose we want to impose constraints on  $\phi_1$  at certain specified positions  $\Gamma_1$  within  $\Omega$ , expressed as

$$\phi_1|_{\Gamma_1} = \bar{C}_1 \quad \text{at } \Gamma_1. \quad (\text{B.12})$$

We can use the Lagrange multiplier method to introduce a set of multipliers  $\lambda_i$  (which are additional global unknowns but only act at the “constraint point”), and construct the following augmented energy functional:

$$\mathcal{L}(\phi_1, \phi_2, \lambda) = \mathcal{E}(\phi_1, \phi_2) + \sum_{i=1}^m \lambda_i [\phi_1(x_i) - c_i] \quad (\text{B.13})$$

$x_i \in \Omega$  are the discrete points to enforce constraint, given by the set  $\Gamma_1 := \{x_1, x_2, \dots, x_m\}$ .

To derive the extended Euler-Lagrange equations of **Eq. (B.13)**, we take variation of  $\mathcal{L}$  with respect to  $\phi_1$ ,  $\phi_2$ , and  $\lambda$ . Utilizing the respective Euler-Lagrange equations of  $\mathcal{E}(u_1, u_2)$ , we can obtain the following extended Lagrange system:

$$\nabla \cdot (-\sigma \nabla \phi_1) + f + \sum_{i=1}^m \lambda_i \delta(x - x_i) = 0 \quad \text{in } \Omega \quad (\text{B.14a})$$

$$\nabla \cdot (-\kappa \nabla \phi_2) - f = 0 \quad \text{in } \Omega \quad (\text{B.14b})$$

$$\phi_1(x_i) - c_i = 0 \quad \text{for } x_i \in \Gamma_1 \quad (\text{B.14c})$$

with Neumann conditions given in **Eqs. (B.1c)–(B.1d)**.

Here,  $\delta(x - x_i)$  is Dirac delta function, meaning  $\lambda_i$  effects the system only at  $x_i$ .

## Appendix C Line Search Method for Reference Potential Matching

To refine the reference potential  $c_l$  for the electrolyte domain, we employ a gradient descent-based line search methods within an optimization framework. This iterative approach aims to minimize the objective function  $J$ , as defined in **Eq. (18)**, ensuring that the solution adheres to charge conservation. Gradient descent updates the reference potential by moving in the direction of the negative gradient of the objective function. The gradient is computed using a finite-difference approximation:

$$\nabla J(c_l) \approx \frac{J(c_l + \delta) - J(c_l)}{\delta} \quad (\text{C.1})$$

Alternatively, central finite differences can be used for higher accuracy, given by:

$$\nabla J(c_l) \approx \frac{J(c_l + \delta) - J(c_l - \delta)}{2\delta} \quad (\text{C.2})$$

where  $\delta$  is a small perturbation. The iterative update rule is:

$$c_l^{(k+1)} = c_l^{(k)} - \beta \nabla J(c_l^{(k)}) \quad (\text{C.3})$$

where  $\beta > 0$  is the step size. To ensure convergence, the step size is adjusted using the Armijo condition:

$$J(c_l^{(k+1)}) \leq J(c_l^{(k)}) + c\beta \nabla J(c_l^{(k)})(-\nabla J(c_l^{(k)})) \quad (\text{C.4})$$

where  $c \in (0, 1)$  is a small constant, and  $\beta$  is initialized to a default value and iteratively adjusted as follows: 1. Start with an initial  $\beta > 0$ . 2. Reduce  $\beta$  by a factor of  $\rho \in (0, 1)$  (e.g.,  $\rho = 0.5$ ) until the Armijo condition is met. 3. Use the updated  $\beta$  for the next iteration.

## Appendix D Exact Solution Expression of Eq. 31

We use the First Integral Method to find the exact solution of Eq. 31 in 1D under galvanostatic and potentiostatic conditions.

### Step 1: First Integral

The given PDE is:

$$\frac{d^2\eta}{dx^2} = a' \sinh(b\eta). \quad (\text{D.1})$$

Multiply both sides by  $\frac{d\eta}{dx}$  to prepare for integration:

$$\frac{d^2\eta}{dx^2} \frac{d\eta}{dx} = a' \sinh(b\eta) \frac{d\eta}{dx} \quad (\text{D.2})$$

Rewriting the left-hand side as a total derivative:

$$\frac{d}{dx} \left( \frac{1}{2} \left( \frac{d\eta}{dx} \right)^2 \right) = \frac{d}{dx} \left( \frac{a'}{b} \cosh(b\eta) \right) \quad (\text{D.3})$$

Integrate both sides once:

$$\frac{1}{2} \left( \frac{d\eta}{dx} \right)^2 = \frac{a'}{b} \cosh(b\eta) + C \quad (\text{D.4})$$

where  $C$  is the integration constant.

Then, we use the Neumann boundary conditions to determine  $C$ .

### Step 2: Apply Boundary Conditions

At  $x = 0$ :

$$\frac{1}{2} q_1^2 = \frac{a'}{b} \cosh(b\eta_0) + C \quad (\text{D.5})$$

At  $x = W$ :

$$\frac{1}{2} q_2^2 = \frac{a'}{b} \cosh(b\eta_W) + C \quad (\text{D.6})$$

where  $q_1 = \frac{d\eta}{dx}(0)$ ,  $q_2 = \frac{d\eta}{dx}(W)$ ,  $\eta_0 = \eta(0)$  and  $\eta_W = \eta(W)$ . We can use either boundary equation to find the expression for  $C$ , such that:

$$C = \frac{1}{2} q_1^2 - \frac{a'}{b} \cosh(b\eta_0) \quad (\text{D.7})$$

### Step 3: Solve for $x$

Rearrange:

$$\frac{d\eta}{dx} = \sqrt{\frac{2a'}{b} \cosh(b\eta) + q_1^2 - \frac{2a'}{b} \cosh(b\eta_0)}. \quad (\text{D.8})$$

Separating variables:

$$dx = \frac{d\eta}{\sqrt{\frac{2a'}{b} \cosh(b\eta) + q_1^2 - \frac{2a'}{b} \cosh(b\eta_0)}}. \quad (\text{D.9})$$

Integrate:

$$x = \int_{\eta_0}^{\eta} \frac{d\eta}{\sqrt{\frac{2a'}{b} \cosh(b\eta) + q_1^2 - \frac{2a'}{b} \cosh(b\eta_0)}}. \quad (\text{D.10})$$

This defines an implicit relation between  $x$  and  $\eta(x)$ , which needs to be evaluated numerically as we end up with an integral problem. We can then apply numerical integration or approximate using elliptic functions.

## References

- [1] S. Santhanagopalan and R.E. White. Electrodes — porous electrodes. In Jürgen Garche, editor, *Encyclopedia of Electrochemical Power Sources*, pages 110–120. Elsevier, Amsterdam, 2009.

- [2] John Newman and Nitash P Balsara. *Electrochemical systems*. John Wiley & Sons, 2021.
- [3] Richard Alkire and Brian Gracon. Flow-through porous electrodes. *Journal of the Electrochemical Society*, 122(12):1594, 1975.
- [4] Zhenghui Pan, Jie Yang, Junhua Kong, Xian Jun Loh, John Wang, and Zhaolin Liu. “Porous and yet dense” electrodes for high-volumetric-performance electrochemical capacitors: Principles, advances, and challenges. *Advanced Science*, 9(4):2103953, 2022.
- [5] Hamid Hamed, Lowie Henderick, Behnam Ghalami Choobar, Jan D’Haen, Christophe Detavernier, An Hardy, and Mohammadhosein Safari. A limitation map of performance for porous electrodes in lithium-ion batteries. *Iscience*, 24(12), 2021.
- [6] Deyang Qu. Fundamental principals of battery design: Porous electrodes. In *AIP Conference Proceedings*, volume 1597, pages 14–25. American Institute of Physics, 2014.
- [7] Raymond B Smith and Martin Z Bazant. Multiphase porous electrode theory. *Journal of The Electrochemical Society*, 164(11):E3291, 2017.
- [8] Duo Zhang, Antoni Forner-Cuenca, Oluwadamilola O Taiwo, Vladimir Yufit, Fikile R Brushett, Nigel P Brandon, Sai Gu, and Qiong Cai. Understanding the role of the porous electrode microstructure in redox flow battery performance using an experimentally validated 3d pore-scale lattice boltzmann model. *Journal of Power Sources*, 447:227249, 2020.
- [9] John Newman and William Tiedemann. Porous-electrode theory with battery applications. *AIChE Journal*, 21(1):25–41, 1975.
- [10] Kiana Amini, Amin Sadeghi, Mark Pritzker, and Jeff Gostick. Porous electrodes in redox flow batteries. In Luisa F. Cabeza, editor, *Encyclopedia of Energy Storage*, pages 466–479. Elsevier, Oxford, 2022.
- [11] Allen J Bard, Larry R Faulkner, and Henry S White. *Electrochemical methods: fundamentals and applications*. John Wiley & Sons, 2022.
- [12] Justin C Bui, Eric W Lees, Lalit M Pant, Iryna V Zenyuk, Alexis T Bell, and Adam Z Weber. Continuum modeling of porous electrodes for electrochemical synthesis. *Chemical reviews*, 122(12):11022–11084, 2022.
- [13] Jakub K Włodarczyk, Gaël Mourouga, Roman P Schärer, and Jürgen O Schumacher. Continuum modelling and simulation of flow batteries. *Flow Batteries: From Fundamentals to Applications*, 1:379–412, 2023.
- [14] Dongjiang You, Huamin Zhang, and Jian Chen. A simple model for the vanadium redox battery. *Electrochimica Acta*, 54(27):6827–6836, 2009.
- [15] Deepak Krishnamurthy, Erik O Johansson, Jin Wook Lee, and Erik Kjeang. Computational modeling of microfluidic fuel cells with flow-through porous electrodes. *Journal of Power Sources*, 196(23):10019–10031, 2011.
- [16] IM Bayanov and R Vanhaelst. The numerical simulation of vanadium redox flow batteries. *Journal of mathematical chemistry*, 49:2013–2031, 2011.

- [17] Edmund JF Dickinson and Andrew J Wain. The butler-volmer equation in electrochemical theory: Origins, value, and practical application. *Journal of Electroanalytical Chemistry*, 872:114145, 2020.
- [18] Piergiorgio Alotto, Massimo Guarnieri, and Federico Moro. Redox flow batteries for the storage of renewable energy: A review. *Renewable and sustainable energy reviews*, 29:325–335, 2014.
- [19] Grigory I Barenblatt, Iu P Zheltov, and IN Kochina. Basic concepts in the theory of seepage of homogeneous liquids in fissured rocks [strata]. *Journal of applied mathematics and mechanics*, 24(5):1286–1303, 1960.
- [20] Yuhe Wang and Yating Wang. Physical similarity of fluid flow in bimodal porous media: Part 1–basic model and solution characteristics. *arXiv preprint arXiv:2408.16434*, 2024.
- [21] H H Gerke and M Th Van Genuchten. A dual-porosity model for simulating the preferential movement of water and solutes in structured porous media. *Water resources research*, 29(2):305–319, 1993.
- [22] Todd Arbogast. Computational aspects of dual-porosity models. In *Homogenization and porous media*, pages 203–223. Springer, 1997.
- [23] I Yucel Akkutlu, Yalchin Efendiev, Maria Vasilyeva, and Yuhe Wang. Multiscale model reduction for shale gas transport in a coupled discrete fracture and dual-continuum porous media. *Journal of Natural Gas Science and Engineering*, 48:65–76, 2017.
- [24] Min Wang, Siu Wun Cheung, Eric T Chung, Maria Vasilyeva, and Yuhe Wang. Generalized multiscale multicontinuum model for fractured vuggy carbonate reservoirs. *Journal of Computational and Applied Mathematics*, 366:112370, 2020.
- [25] Tomas Vogel, Jan Brezina, Michal Dohnal, and Jaromir Dusek. Physical and numerical coupling in dual-continuum modeling of preferential flow. *Vadose Zone Journal*, 9(2):260–267, 2010.
- [26] Rolando Guidelli, Richard G Compton, Juan M Feliu, Eliezer Gileadi, Jacek Lipkowski, Wolfgang Schmickler, and Sergio Trasatti. Defining the transfer coefficient in electrochemistry: An assessment (iupac technical report). *Pure and Applied Chemistry*, 86(2):245–258, 2014.
- [27] Wolfgang Dreyer, Clemens Gohlke, and Rüdiger Müller. A new perspective on the electron transfer: recovering the butler–volmer equation in non-equilibrium thermodynamics. *Physical Chemistry Chemical Physics*, 18(36):24966–24983, 2016.
- [28] J Raphael Seidenberg, Alexander Mitsos, and Dominik Bongartz. Interpreting concentration and activation overpotentials in electrochemical systems: A critical discussion. *Journal of The Electrochemical Society*, 172(4):043506, 2025.
- [29] Qian Xu and TS Zhao. Fundamental models for flow batteries. *Progress in Energy and Combustion Science*, 49:40–58, 2015.
- [30] Yasser Ashraf Gandomi, DS Aaron, TA Zawodzinski, and MM Mench. In situ potential distribution measurement and validated model for all-vanadium redox flow battery. *Journal of The Electrochemical Society*, 163(1):A5188, 2015.

- [31] Yunxiang Chen, Jie Bao, Zhijie Xu, Peiyuan Gao, Litao Yan, Soowhan Kim, and Wei Wang. A hybrid analytical and numerical model for cross-over and performance decay in a unit cell vanadium redox flow battery. *Journal of Power Sources*, 578:233210, 2023.
- [32] Akeel A Shah, MJ Watt-Smith, and FC Walsh. A dynamic performance model for redox-flow batteries involving soluble species. *Electrochimica Acta*, 53(27):8087–8100, 2008.
- [33] Joseba Martinez Lopez, Iñigo Aramendia, Unai Fernandez-Gamiz, Eduardo Sanchez-Diez, Aitor Beloki, Erol Kurt, and Jose Manuel Lopez-Guede. Computational modeling of a 2d vanadium redox flow battery cell. *JOM*, 76(1):130–140, 2024.
- [34] COMSOL AB. *COMSOL Multiphysics Documentation*, 2023. Version 6.1, COMSOL AB, Stockholm, Sweden.
- [35] Rudolph A Marcus. Electron transfer reactions in chemistry theory and experiment. *Journal of Electroanalytical Chemistry*, 438(1-2):251–259, 1997.
- [36] Tulong Zhu and SN1633725 Atluri. A modified collocation method and a penalty formulation for enforcing the essential boundary conditions in the element free galerkin method. *Computational Mechanics*, 21(3):211–222, 1998.
- [37] Alfio Quarteroni and Alberto Valli. *Numerical approximation of partial differential equations*. Springer, 1994.
- [38] J Frédéric Bonnans, J Charles Gilbert, Claude Lemaréchal, and Claudia A Sagastizábal. *Numerical optimization: theoretical and practical aspects*. Springer, 2006.
- [39] Adi Ben-Israel and Thomas NE Greville. *Generalized inverses: theory and applications*. Springer, 2003.
- [40] Gene H Golub and Charles F Van Loan. *Matrix computations*. JHU press, 2013.
- [41] Gene H Golub, Per Christian Hansen, and Dianne P O’Leary. Tikhonov regularization and total least squares. *SIAM journal on matrix analysis and applications*, 21(1):185–194, 1999.
- [42] João Carlos Alves Barata and Mahir Saleh Hussein. The moore–penrose pseudoinverse: A tutorial review of the theory. *Brazilian Journal of Physics*, 42:146–165, 2012.
- [43] Christopher C Paige and Michael A Saunders. Solution of sparse indefinite systems of linear equations. *SIAM journal on numerical analysis*, 12(4):617–629, 1975.
- [44] David Chin-Lung Fong and Michael Saunders. Lsmr: An iterative algorithm for sparse least-squares problems. *SIAM Journal on Scientific Computing*, 33(5):2950–2971, 2011.
- [45] Christopher C Paige and Michael A Saunders. Lsqsr: An algorithm for sparse linear equations and sparse least squares. *ACM Transactions on Mathematical Software (TOMS)*, 8(1):43–71, 1982.
- [46] Arindam Ghosh and Sarit Maitra. The first integral method and some nonlinear models. *Computational and Applied Mathematics*, 40(3):79, 2021.
- [47] Uri M Ascher, Robert MM Mattheij, and Robert D Russell. *Numerical solution of boundary value problems for ordinary differential equations*. SIAM, 1995.

- [48] William H Press. *Numerical recipes 3rd edition: The art of scientific computing*. Cambridge university press, 2007.